Interface Focus

Lighting up cells with lanthanide self-assembled helicates

Jean-Claude G. Bünzli

Interface Focus 2013 **3**, 20130032, published 23 August 2013

Interface Focus

rsfs.royalsocietypublishing.org

Review

Cite this article: Bünzli J-CG. 2013 Lighting up cells with lanthanide self-assembled helicates. Interface Focus 3: 20130032. http://dx.doi.org/10.1098/rsfs.2013.0032

One contribution of 6 to a Theme Issue 'Photons and biology'.

Subject Areas:
biochemistry, chemical physics

Keywords:
lanthanide, luminescent bioprobe, self-assembly, cell imaging, time-resolved luminescence microscopy, bioconjugate

Author for correspondence:
Jean-Claude G. Bünzli
e-mail: jean-claude.bunzli@epfl.ch

Lighting up cells with lanthanide self-assembled helicates

Jean-Claude G. Bünzli

Institute of Chemical Sciences and Engineering, École Polytechnique Fédérale de Lausanne, BCH 1402, 1015 Lausanne, Switzerland

Lanthanide bioprobes and bioconjugates are ideal luminescent stains in view of their low propensity to photobleaching, sharp emission lines and long excited state lifetimes permitting time-resolved detection for enhanced sensitivity. We show here how the interplay between physical, chemical and biochemical properties allied to microfluidics engineering leads to self-assembled dinuclear lanthanide luminescent probes illuminating live cells and selectively detecting biomarkers expressed by cancerous human breast cells.

1. Introduction

A key challenge in biology and medicine is to gain information on the structural and functional properties of cells, organs and living organisms. Imaging techniques are crucial tools towards this goal, and the development of trustable diagnostic imaging techniques such as positron emission tomography, X-ray computed tomography, X-ray angiography, magnetic resonance imaging or ultrasound imaging, and of their associated contrast agents, has had a tremendous impact on the progress of medicine over the past 30 years, particularly with respect to cancer detection and treatment. Despite the impressive panoply of available high-tech imaging tools, there is still much space for improvements, especially when it comes to spatial resolution, sensitivity and penetration depth. Present efforts focus on several aspects, for instance, *theranostics* which combines drug delivery with a diagnostic agent [1] or *molecular imaging* which aims at gaining target-specific information with high sensitivity. To fulfil the requirements associated with these technologies, it appears necessary to design probes mixing different modalities and/or signal processing protocols [2].

Luminescence imaging emerges as an essential component among the various technologies required to meet the stringent constraints of modern diagnostics and therapy [3,4]. Indeed, depending on its wavelength, light can penetrate deeply within biological tissues and its detection is highly sensitive, because single-photon spectroscopy is achievable. Another advantage is that photons interact with electrons at the molecular level and techniques such as Förster resonant energy transfer (FRET) lead to sensitive detection of molecular interactions, for example, DNA hybridization or biomarker recognition. Moreover, depending on the lifetime of the excited state generating light, time-domain information can be gained, thanks to time-gated detection. Finally, because quantum yields are temperature-dependent, recording of luminescence intensity variations within cells or tissues results in thermal sensing and/or imaging [5]. There are essentially four types of optical luminescent bioprobes.

(i) The first category consists of well-documented and highly fluorescent organic luminophores which are easy to derivatize for gaining specificity, for example, cell-penetrating agents localizing in given organelles or bioconjugated chromophores for antigen detection. Two major disadvantages of organic chromophores are their very short excited state lifetimes and their sensitivity to photobleaching. The first drawback renders time-resolved detection (TRD), which considerably enhances signal-to-noise ratio (SNR) by offsetting the probe autofluorescence, difficult to implement, because it necessitates sophisticated and expensive experimental set-ups.

The second shortcoming translates into operative times which can be as short as a few seconds only, a rather small time window for informative imaging.

(ii) Fluorescent proteins, of which the archetype is the green fluorescent protein discovered in *Aequorea victoria* medusa, which emits at 505 nm, and which revolutionized microscopy [6,7]. The main advantages of this protein are its low phototoxicity when compared with small organic molecules such as fluorescein isothiocyanate, and the fact that derivatives (mutants, fusion with other proteins) can be easily engineered, leading to specific detection. On the other hand, it suffers the same problems outlined above for organic dyes and, in addition, its large size may hinder protein–protein interactions in cellular environments [8].

(iii) A second type of chromophores encompasses semiconductor quantum dots (QDs) and their bioconjugates which are becoming a dominant class of imaging probes. QDs are highly luminescent with fairly sharp (full width at half height (fwhh) of 25–100 nm) emission bands ranging from 450 to 1250 nm depending on the nanocrystal size and they display better photostability than organic chromophores [9]. The disadvantages evidenced in the early experiments, namely large particle size (10–30 nm) and blinking behaviour which interrupts fluorescence for variable times, have the tendency to be cured presently, thanks to better synthetic methods [10]. On the other hand, concerns about toxicity of the heavy elements they are made of and of the free radicals generated consecutively to their use remain present [11].

(iv) Finally, d-transition metal ions [12,13] and trivalent lanthanide ions, Ln^{III} [14,15], represent valuable substitutes to both organic luminophores and QDs. This originates from their remarkable optical properties, featuring long excited state lifetimes and, for Ln^{III} derivatives, narrow absorption and emission bands with energies showing small dependence on the chemical environment of the ion. As a result, Ln^{III} ions have been taken advantage of in numerous applications [16], in particular, in biosciences. Indeed, both spectral and time discrimination of their emission bands, which extend from UV through near-infrared (NIR) spectral ranges depending on the ion, can be implemented with basic and low-cost instrumentation. Another noteworthy and decisive advantage of lanthanide compounds is their low sensitivity to photobleaching, because their luminescence is sensitized via the organic ligands and energy transfer from the chromophore to the Ln^{III} ion is fast enough to avoid photodegradation of the ligand [17]. While nanoparticles and nanocomposites are rapidly changing the landscape of bioreporters for sensing and imaging [18], molecular complexes remain in widespread use, and, in the following sections, we exclusively focus on the latter bioprobes and their conjugates.

The use of time-resolved luminescence (TRL) coupled with lanthanide probes for bioanalyses was pioneered by Hemmilä and co-workers [19,20] at the end of the 1970s who proposed to replace radioactivity-based immunoassays with luminescence immunoassays. These analyses are now ubiquitous in medical and biological laboratories. Examples are testing for early stage of pregnancy by quantifying the human chorionic gonadotropin hormone, detecting the human immunodeficiency virus, or measuring the prostate-specific antigen level in blood or urine. Lanthanide complexes, polyaminocarboxylates or macrocyclic complexes, are attached onto a specific antibody, and luminescence from the emitting ion is detected after the biochemical reaction is completed, either in a two-step procedure (heterogeneous assays) or with a one-step, FRET-based, protocol (homogeneous assays) [15]. The field is the subject of numerous review articles appearing regularly [15,21] and it has sustained an unprecedented growth with the appearance of nanoprobes [22]. Initially, Ln^{III} ions or complexes were simply doped into silica nanoparticles further derivatized with avidin, biotin or an antibody [23]. However, the need for UV/blue excitation which may be detrimental to live cells has led to the development of bioprobes based on upconversion nanoparticles (UCNPs) [24,25]. The latter usually consist of a sensitizer, typically Yb^{III} absorbing at 980 nm, that is at a wavelength at which biological tissues are transparent, and of an emitter such as Er^{III} or Tm^{III} with luminescence in the visible or onset of the NIR spectral ranges; the upconverting nanophosphors can also be provided in light-responsive systems which release payloads upon NIR excitation [26]. Alternatively, long-persistence luminescent nanophosphors have lifetimes long enough so that excitation may be conducted prior to the introduction of the biolabel into the sample to be assayed or imaged [27].

As the success story of lanthanide-based bioanalyses unfolded, attempts to use these probes for bioimaging were a logical follow up. Attention has been focused on both *in vitro* and *in vivo* imaging, and several solutions have been proposed for improving the SNR of the images. In the case of *in vivo* imaging, probes excitable and emitting in the NIR have been proposed, e.g. Nd^{III}-doped $NaGdF_4$ nanoparticles [28] or Yb^{III} complexes amenable to multi-photon excitation [29]. On the other hand, *in vitro* imaging or sensing, particularly of fixed cells or tissues, is less compelling with respect to phototoxicity and many lanthanide coordination compounds revealed to be efficient 'optical contrast agents' [30,31]; the luminosity of such probes can be increased if dendrimeric ligands are used [32].

In this review, we concentrate on one class of luminescent lanthanide bioprobes, namely dinuclear helicates which meet the chemical, physical and biochemical requirements for *in vitro* staining of live cells and for the detection of biomarkers. We show how combining TRD with laboratory-on-a-chip technology leads to highly sensitive and selective recognition of biomarkers expressed by human cancerous cells and tissues.

2. Time-resolved luminescence microscopy

Intrinsically, quantitative measurement of luminescence intensity is more sensitive than measurement of light absorption, especially when weak signals are concerned. Very sensitive photomultipliers operated in photon-counting mode, or CCD cameras detect a few photons per second when the dark noise is reduced by cooling the photocathode. With respect to microscopy, luminescence recording of the image results in enhanced contrast, comparable with the one obtained by conventional techniques associated with classical optical microscopy, for example, oblique, cross-polarized or darkfield illumination. In luminescence microscopy, luminescent stains are introduced into the sample, and emission is stimulated

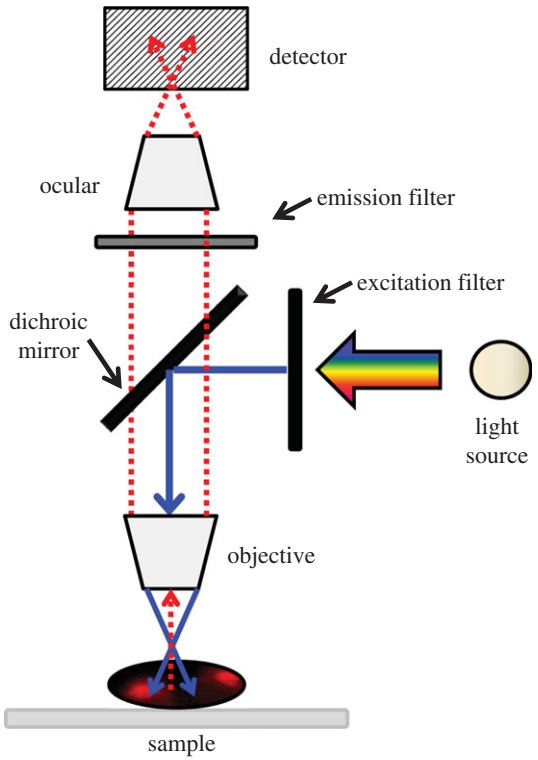

Figure 1. Simplified scheme of an epifluorescence microscope used for luminescence microscopy.

by an incident beam of light. These stains are fluorescent organic molecules, phosphorescent transition metal complexes, QDs, doped nanoparticles or their bioconjugates for improved specificity. However, staining may interfere with the cell functions or even may need fixing the cells; in any case, cytotoxicity and morphology tests should be performed to detect unwanted effects.

In life sciences, the experimental set-up corresponds usually to an *epifluorescence* microscope in which the excitation light is directed onto the sample from above after going through a dichroic mirror and the objective (figure 1). The excitation wavelength is selected through adequate choices of the dichroic mirror and the excitation filter. The light emitted by the sample is focused onto the detector through the objective used for excitation, and the spectral range is selected by the emission filter. A great deal of the excitation light is transmitted by the sample, so that only reflected light accompanies sample fluorescence, and the SNR is large, especially that the emission filter can help eliminate spurious excitation light. The light source can be non-coherent (e.g. xenon lamp) or coherent (e.g. laser, diode laser), polarized or un-polarized depending on the effect sought for.

The photometric throughput of a luminescence microscope is estimated as follows assuming linear isotropic response and not too intense illumination to avoid saturation [33]. Excitation light with wavelength λ is absorbed by the chromophores in the object field with a probability governed by the absorption cross section $\sigma_A(\lambda)$ (in cm^2 molecule^{-1}) defined as

$$\sigma_A(\lambda) = 10^3 \ln(10)\frac{\varepsilon_\lambda}{N} = 3.82 \times 10^{-21}\,\varepsilon(\lambda), \qquad (2.1)$$

where $\varepsilon(\lambda)$ is the molar absorption coefficient (M^{-1} cm^{-1}) and N Avogadro's number (molecule mol^{-1}). The usefulness of the cross section is easy to understand: it avoids defining an absorption path length in the sample. In addition to $\varepsilon(\lambda)$, chromophores are characterized by their quantum yield $Q(\lambda_{exc}, \lambda)$ and act as secondary isotropic light sources with spectral radiant intensity $I(\lambda)$:

$$I(\lambda) = \frac{I_{exc}(\lambda)\sigma_A(\lambda)Q(\lambda_{exc}, \lambda)q(\lambda)}{4\pi}, \qquad (2.2)$$

where $I_{exc}(\lambda)$ is the excitation irradiance (W cm^{-2}), and $q(\lambda)$ is the spectral distribution function, which is related to the emission spectrum corrected for the instrumental function, $I_{corr}(\lambda)$:

$$q(\lambda) = \frac{\lambda I_{corr}(\lambda)}{\int \lambda I_{corr}(\lambda)\mathrm{d}\lambda}. \qquad (2.3)$$

Calculation of the signal intensity at the detector must take into account the solid angle of collection for the chromophore embedded into a medium with refractive index n and acting as a non-Lambertian diffuse point source. This solid angle is equal to

$$2\pi\left(1 - \sqrt{1 - \left(\frac{\mathrm{NA}}{n}\right)^2}\right), \qquad (2.4)$$

where NA is the aperture number and n the refractive index. Further assuming an overall transmittance $\tau_{opt}(\lambda)$ of the entire optical set-up, a measuring spectral bandwidth $\Delta\lambda_{em}$, and a spectral sensitivity (response) $\eta_{det}(\lambda)$ of the detector, one finally gets the photoelectron flux ϕ_{im} (in photoelectrons s^{-1} molecule^{-1}) in the image plane taking into account that the energy of a photon with wavelength λ is $1.987 \times 10^{-16}/\lambda$ J $\approx 2 \times 10^{-16}/\lambda$ J:

$$\Phi_{im} = 10^{16} Q(\lambda_{exc}, \lambda) \cdot [I_{exc}\sigma_A(\lambda)] \cdot [q(\lambda)\Delta\lambda_{em}] \times \left(1 - \sqrt{1 - \left(\frac{\mathrm{NA}}{n}\right)^2}\right) \cdot \left[\tau_{opt}(\lambda)\eta_{det}(\lambda)\frac{\lambda}{4}\right], \qquad (2.5)$$

with quantities between brackets having to be evaluated by integration over the entire spectral range. As an example, a xenon lamp source delivering 25 W cm^{-2} at the specimen and a 63× objective with numerical aperture NA = 1.3 result in the emission of 25 photoelectrons s^{-1} molecule^{-1} provided $Q(\lambda_{exc}, \lambda)$ is large.

There are various techniques for recording luminescence microscopy images and for improving the contrast and/or the resolution. A commonly used one is *confocal microscopy* in which conventional wide-field illumination is replaced by spot laser illumination. A scanning unit is inserted between the dichroic mirror and the objective, and allows the illumination of successive points on the sample. In addition, a pinhole is introduced in front of the detection assembly for eliminating out-of-focus light rays. The name 'confocal' stems from the fact that only light emitted very close to the focal plane in the sample can be detected. The set-up results in increased optical resolution, though to the cost of signal intensity so that reconstructed two- or three-dimensional images require long exposure times. Confocal microscopy is now often combined with multi-photon excitation which protects live samples from photodegradation by irradiation in the NIR instead of in the visible spectral range; this also results in deeper penetration of the excitation light into the sample [34].

A major problem affecting luminescence microscopy is that both organic and inorganic chromophores are ubiquitous in nature; UV or visible excitation therefore provokes an intense luminescence stemming from the sample and its containment. This so-called *autofluorescence* severely obscures

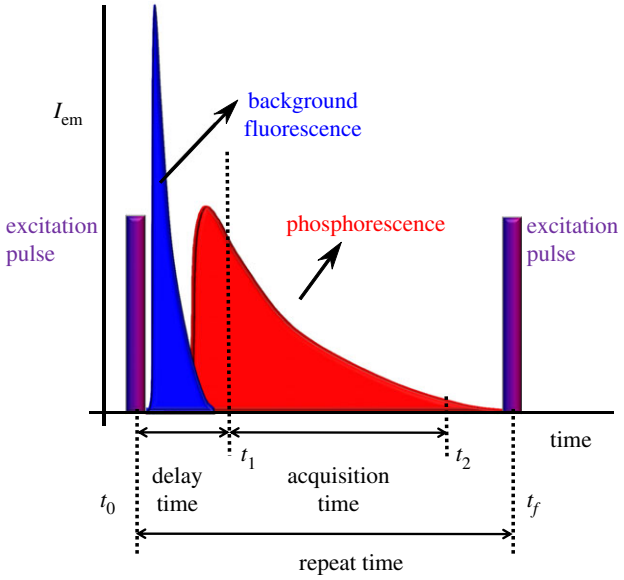

Figure 2. Principle of time-resolved luminescence and definition of essential parameters.

the emission from the chromophoric probe. A clever selection of filters and dichroic mirror may reduce the problem, but it never eradicates it. This difficulty can be circumvented if pulsed excitation is used and if images are produced based on the differences in exponential decays of the luminescent stain and the autofluorescence. In the case of organic fluorophores, this is usually achieved by means of time-correlated single-photon counting with resolution down to a few picoseconds or by phase modulation when fluorescence lifetimes are determined in the frequency domain by phase-modulated detection. However, the instrumental set-up is relatively sophisticated, and a way must be found for transferring rapidly all of the data stored in the camera [35], so that another solution is emerging: luminescence imaging with phosphorescent bioprobes. Autofluorescence occurs in a short span of time (typically in the nanosecond range), so that simple time-resolved (or time-gated) detection can be applied. The microscope is then operated in time domain and detects only the longer time-scale events. The principle of this powerful technique is outlined in figure 2.

Pulsed illumination is achieved either by a pulsed light source (flash lamp, laser) or by modulating a continuous light beam with a chopper or a ferroelectric shutter. The detector is gated, that is, turned on or off depending on the advancement of the experiment. The initial pulse defines $t(0)$; at that time, the detector is off. Intense autofluorescence is generated, and the detector is maintained off until it disappears (gate or delay time). Phosphorescence from the luminescent probe develops more slowly, and the detector captures it until it fades out (acquisition time). At that point, the detector is again shut off, and a new light pulse is shined onto the sample, restarting the cycle. Referring to lanthanide luminescent probes, the entire experiment lasts about 1–4 ms, so that light measurement can be theoretically repeated up to approximately 500 times per second, although practically the repetition rate depends on the characteristics of the pulsed source. Both delay and acquisition times have to be chosen carefully in order to maximize the SNR. For instance, a very long delay time cuts out the most intense emission from the phosphorescent probe, and a very long acquisition time leads to noise integration at the end of the decay. If the luminescent probe decay is a single-exponential function, then the phosphorescence signal intensity decreases as

Table 1. Rounded proportions (%) of the total emission intensity as a function of delay (t_1) and acquisition (t_2) times for a normalized single-exponential luminescence decay with lifetime τ and $B = 0$; see equation (2.6). Shading points to 'ideal' conditions.

$t_1/\tau \rightarrow$ $t_2/\tau \downarrow$	0.0	0.1	0.2	0.5	1.0	2.0
1	63	54	45	24	0	0
2	87	77	68	47	23	0
3	95	86	77	56	32	9
4	98	89	80	59	35	12
5	99	90	81	60	36	13

$$I_{em} = I^0_{em} \times e^{-t/\tau} + B, \tag{2.6}$$

where τ is the excited-state lifetime of the chromophore and B is the background noise. Proportions of the total emission signal measured versus gate and acquisition times are collected in table 1. From these simulated data, it is clear that the delay time should not be longer than 0.5 τ, whereas detecting light emitted after 3–4τ does not bring much signal improvement. Visible-emitting Ln^{III} ions such as Eu^{III} or Tb^{III} have lifetimes in the range 0.5–2.5 ms so that, ideally, t_1 should be in the range 50–250 µs and t_2 in the range 1.5–7.5 ms. Because most of the TRL microscopes used to date are modifications of epifluorescence microscopes and are fitted with a combination of a fast switching pulsed light-emitting diode and a chopper [36], long acquisition times can be implemented. Reported windows are, however, in the range 0.1–5 ms only, which explains why actual improvements are less than predicted. Nevertheless sizeable and bettering in SNR of the order of 20–30 times are regularly reported [36,37].

Another point stemming from table 1 is that, ideally, the delay and acquisition times should be adapted to the decay time of the luminescent probe. This is not very easy with chopper-fitted microscopes, because these times not only depend on the rotation speed of the chopper but also on the number of blades. Optimum working conditions would therefore require changing the chopper wheel, depending on the luminescent stain, which is not very practical. Microscopes are therefore usually fitted with chopper wheels adequate for one class of lanthanide luminescent probes (e.g. polyaminocarboxylates, with lifetimes around 600–700 µs). There are other ways of continuously modifying the time delay, some have also their drawbacks [31] but it seems that a new generation of light-emitting diodes (SpectraLED from Horiba) will impose themselves as adequate pulsed light sources for phosphorescence lifetime measurements. These low-cost light-emitting diodes deliver pulses tunable between 0.1 µs and several ms, cover the spectral range 355–1275 nm, can operate at high repetition rates and have no afterglow, which permits more reliable determination of lifetimes shorter than 100 µs.

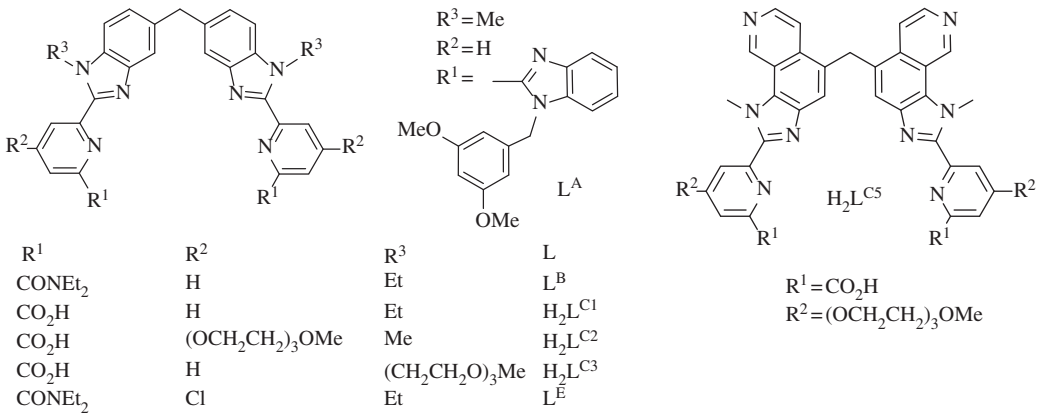

R^1	R^2	R^3	L
$CONEt_2$	H	Et	L^B
CO_2H	H	Et	H_2L^{C1}
CO_2H	$(OCH_2CH_2)_3OMe$	Me	H_2L^{C2}
CO_2H	H	$(CH_2CH_2O)_3Me$	H_2L^{C3}
$CONEt_2$	Cl	Et	L^E

Scheme 1. Hexadentate, ditopic ligand for the self-assembly of triple-stranded lanthanide helicates.

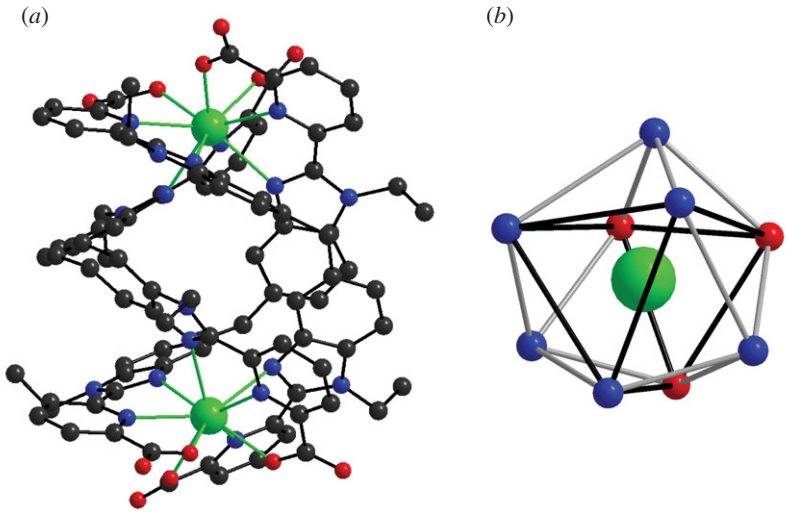

Figure 3. (*a*) Molecular structure of $[Tb_2(L^{C1})_3]$ (H atoms are omitted for clarity). (*b*) Coordination polyhedron showing the slightly distorted tricapped trigonal prismatic arrangement. (Reproduced with permission from Elhabiri *et al*. [46].)

3. Self-assembly of dinuclear lanthanide helicates

Piguet and collaborators reported in 1992 the first dinuclear triple-stranded lanthanide helicate $[Eu_2(L^A)_3]^{6+}$ (scheme 1), a true supramolecular entity, because the molecular framework is stabilized by π-stacking interactions between the ligand strands [38]. This opened the way to a new class of lanthanide polynuclear and polymetallic complexes with extensions, including heterobimetallic 4f–4f′ [39,40] and *n*d–4f [41,42] complexes, as well as tri- and tetranuclear homometallic and heterometallic entities, among others [42,43]. An interesting feature is that the 2 : 3 helicates are quite stable in organic solutions despite an initially large Coulomb repulsion between the two trivalent cations which lie about 9 Å apart; careful thermodynamic considerations for 3d–4f and 4f–4f–4f helicates, however, show that Ln^{III}–Ln^{III} repulsive energy ($\approx$700 kJ mol^{-1}) is largely compensated by solvation energy, explaining the stability of the edifices [44]. A further development took place in 1998 when water-soluble helicates $[Ln_2(L^{C1})_3]$ were synthesized and shown to be quite stable, with $\log\beta_{23}$ of the order of 26–30 [45]. Crystal structures revealed triple-stranded helicates with nine-coordinate metal ions (Ln = Eu, Tb) well imbedded into the edifice and displaying a distorted tricapped trigonal prismatic coordination geometry (figure 3).

A detailed study of lanthanide-induced paramagnetic shifts (Ln = Ce, Pr, Nd, Sm, Eu, Tb, Er, Tm, Yb; diamagnetic references with Ln = Y, La, Lu) concluded that in D_2O at pD 7.4–8.5, the solution structure is very similar to the solid state structure, with an averaged D_3 molecular symmetry [46].

The mechanism of formation of the $[Eu_2(L^{C1})_3]$ helicate has been established and is depicted in figure 4 [47]; in any case, i.e. in the presence of an excess of ligand or of metal ion, it goes through a crucial 2 : 2 pre-helicate; the crystal structure of such an intermediate, $[Eu_2(CF_3SO_3)_4(H_2O)_2(L^B)_2]^{2+}$, reveals a side by side positioning of the ligand strands, each ligand being coordinated to two Eu^{III} ions located on the same side [48]. The 2 : 2 intermediate is very stable towards dissociation of either Eu^{III} or $(L^{C1})^{2-}$ but it reacts very fast with the third ligand strand which wraps around the two ions, giving birth to the final triple-stranded helicate. The overall formation of the dinuclear helicate is complete after a few seconds.

In the triple-stranded helicates, the two metal ions are well protected from water interaction, hence leading to luminescent entities with quantum yields in water of $0.5 \pm 0.01\%$ for Sm^{III} [49], 24 ± 2 and $1.2 \pm 0.1\%$ for Eu^{III} and Tb^{III}, respectively [43] and $1.8 \pm 0.2\%$ for Yb^{III} in D_2O [50]. Further considering that the edifices are potentially chiral—M and P Cr^{III}–Ln^{III} helices have been isolated [51]—and that 4f–4f′ helicates can be obtained in organic media [39,40], hinting to the possibility of having dual emitting helicates or edifices with optical/

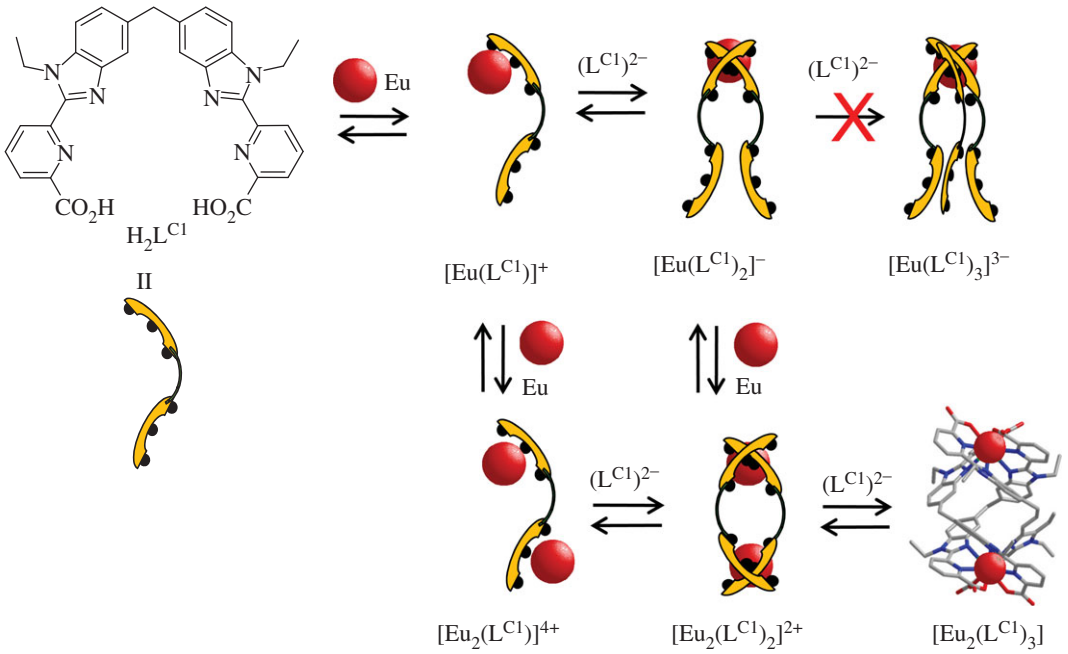

Figure 4. Mechanism of the self-assembly of $[Eu_2(L^{C1})_3]$ in water. (Reproduced with permission from Elhabiri *et al.* [47].)

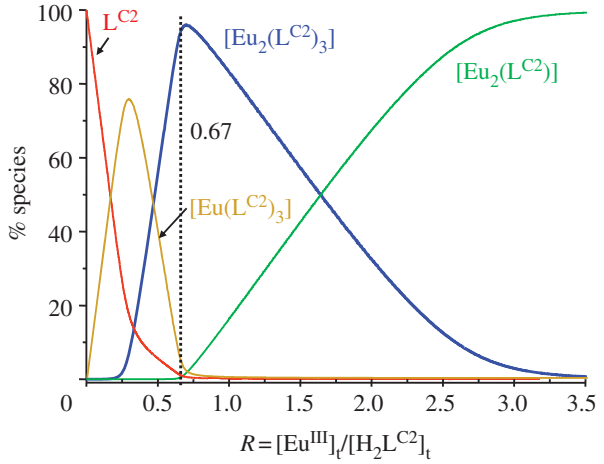

Figure 5. Distribution diagram for $[H_2L^{C2}]_t = 100$ μM. (Reproduced with permission from Chauvin *et al.* [53].)

magnetic properties, we have investigated the opportunity of providing such helicates as probes for cell imaging. To this end, solubility in water and lipophilicity have been improved by grafting short polyoxyethylene chains either on the imidazole units (H_2L^{C3} [52]) or in the four-position of the pyridine units (H_2L^{C2} [53]). The best results have been obtained with the latter and because extending the chain to six (CH_2–CH_2–O) units in $H_2L^{C2'}$ did not bring notable improvements [54] we restrict the discussion to $[Ln_2(L^{C2})_3]$ helicates.

The polyoxyethylene-fitted ligand H_2L^{C2} self-assembles in water at pH 7.4 (Tris–HCl 0.1 M) with Ln^{III} in the same way as H_2L^{C1} yielding triple-stranded helicates with $\log\beta_{23}$ equal to 24.9 ± 0.4, 25.5 ± 0.4 and 26.3 ± 0.4 for La^{III}, Eu^{III} and Lu^{III}, respectively. Other detected species include 1 : 3 and 2 : 1 complexes. The speciation diagram for Eu^{III} is shown in figure 5 for a total ligand concentration of 100 μM. At stoichiometric ratio, the helicate represents 95% of the species in solution (97% if the ligand concentration is increased to 450 μM), that is 2.5% less compared with H_2L^{C1}; however, most of the remaining Eu^{III} is complexed in minor species, so that the concentration of free Eu^{III}, which could be cytotoxic, is negligible. When it comes to bioprobes, not only the thermodynamic stability at physiological pH, but also the kinetic inertness and the effect of pH are important. These parameters have been tested by monitoring the total Eu^{III} luminescence intensity versus time after addition of 100 equivalents of EDTA, diethylenetriaminepentaacetic acid (DTPA), citrate, L-ascorbate or Zn^{II}, or by varying the pH in the 3–10 range. No change in intensity occurred in most cases, the only exceptions being 10% decreases in the presence of DTPA and ascorbate and a 15% decrease in the presence of Zn^{II} [49]. This clearly points to the helicate being more stable than the EDTA complex and of stability comparable with that of the DTPA complex (note that $[Gd(DTPA)]^-$ is used as contrast agent in magnetic resonance imaging of humans). Further experiments within the frame of the use of $[Eu_2(L^{C2})_3]$ as a sensitive analytical probe for DNA showed that Co^{II} and Cu^{II} in 1000-fold excess substantially destroy the helicate [55], but the concentrations used are orders of magnitude larger than those found in living organisms.

In the absence of crystal structure, the symmetry of $[Eu_2(L^{C2})_3]$ was probed by high-resolution luminescence spectroscopy at low temperature, in frozen Tris–HCl/glycerol (9/1 v/v): the emission spectrum (figure 6) is characteristic of a species with slightly distorted trigonal symmetry as shown by the 31 cm^{-1} splitting of the E component of the $^5D_0 \rightarrow {}^7F_1$ transition, and the faint and unique band corresponding to the $^5D_0 \rightarrow {}^7F_0$ transition (fwhh = 17 cm^{-1}). Introduction of the substituent in the four-position of the pyridine rings does not influence much the photophysical properties of the Eu^{III} helicate with respect to $[Eu_2(L^{C1})_3]$, but the electron attractive substituent pushes the ligand states towards slightly higher energy and $[Tb_2(L^{C2})_3]$ becomes notably luminescent, with a quantum yield reaching 11%, whereas the Sm^{III} and Yb^{III} helicates have much smaller quantum yields (table 2), but can nevertheless be used as bioprobes (vide infra).

As a conclusion, the chemical and physical properties of the $[Ln_2(L^{C2})_3]$ helicates perfectly fulfil the requirements for luminescent bioprobes operating in aqueous solution in the pH range 3–10 (some organelles have pH as low as 2!).

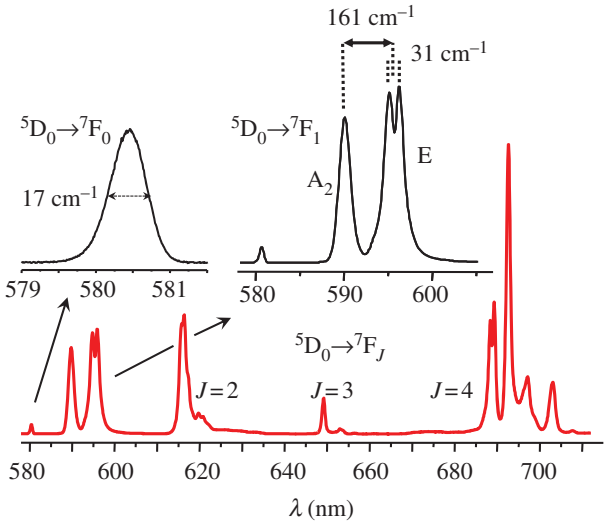

Figure 6. High-resolution emission spectrum of $[Eu_2(L^{C2})_3]$ at 10 K, in frozen Tris–HCl/glycerol (9/1 v/v) under ligand excitation at 341 nm. (Reproduced with permission from Chauvin *et al.* [53].) (Online version in colour.)

Table 2. Quantum yields and lifetimes of the metal excited states for $[Ln_2(L^{Ci})_3]$ helicates ($i = 1-2$) in water at pH 7.4 [49].

helicate	Q_L^{Ln} (%)	τ_{obs} (μs)
$[Sm_2(L^{C1})_3]$	0.5 ± 0.05	42 ± 0.4
$[Eu_2(L^{C1})_3]$	24 ± 2	2400 ± 100
$[Tb_2(L^{C1})_3]$	1.2 ± 0.2	50 ± 0.5
$[Yb_2(L^{C1})_3]$	1.8 ± 0.2[a]	40 ± 2[a]
$[Nd_2(L^{C2})_3]$	n.a.	0.21 ± 0.02
$[Sm_2(L^{C2})_3]$	0.38 ± 0.06	30.4 ± 0.4
$[Eu_2(L^{C2})_3]$	21 ± 2	2400 ± 100
$[Tb_2(L^{C2})_3]$	11 ± 2	650 ± 20
$[Yb_2(L^{C2})_3]$	0.15 ± 0.03	4.40 ± 0.07

[a]Measured in D_2O.

There remains to test whether their biochemical properties are also in line with this function, an assessment which is described in §4.

4. *In vitro* cell imaging

The cytotoxicity of the helicates has been tested by incubating several cell lines in the presence of various concentrations of Eu^{III} chelates and measuring the cell viability by WST-1 assays. These assays concerned Jurkat human T leukaemia, 5D10 mouse hybridoma, MCF-7 human breast carcinoma and HeLa cervical adenocarcinoma cell lines. They were conducted for $[Eu_2(L^{C1})_3]$ [49], $[Eu_2(L^{C2})_3]$ [53] (figure 7) and $[Eu_2(L^{C3})_3]$ [52] with all cell lines and with HeLa cells only for $[Eu_2(L^{C2'})_3]$ [54] and $[Eu_2(L^{C5})_3]$ [57]. No cytotoxicity was evidenced up to 500 μM; owing to its smaller solubility, $[Eu_2(L^{C1})_3]$ was tested only up to 125 μM but was also found to have no influence on cell growth and morphology [49] (figure 7*b*).

Internalization experiments have been conducted with helicates with $(L^{C1})^{2-}$ [49] and $(L^{C3})^{2-}$ (Ln = Eu) [52], $(L^{C2})^{2-}$ (Ln = Sm, Eu, Tb, Yb) [53,56] as well as $(L^{C5})^{2-}$ (Ln = Eu) [57]. All of the tested helicates penetrate into the various cell lines without altering their morphology. Three different imaging experiments are shown in figure 8. Luminescence and confocal images have been recorded according to the experimental conditions described in figure 9, which depicts the transmission of the various filters and of the dichroic mirror in regard of the absorption and emission spectra of $[Eu_2(L^{C2})_3]$: a careful combination of these optical components leads to images with good contrast even for confocal images despite the very small residual absorption at 405 nm; however, one notes for the latter a sizeable background emission at zero concentration of the helicate. This disadvantage vanishes under TRD mode which allows one to identify Eu^{III} luminescence after a short incubation time of 15 min only and with better resolution. Images could be recorded with a helicate concentration as low as 5 μM. The internalization mechanism has been investigated by means of several co-staining experiments [49,56]. The chelates are first taken up in isolated vesicles which diffuse into the cytoplasm and eventually gather around the nucleus, on one side of the cells. The vesicles have sizes ranging from 0.5 to 2 μm. The helicates remain in the vesicles, that is, they do not diffuse into the cytoplasm or nucleus. Co-localization experiments with several organic dyes led to the conclusion that the majority of $[Eu_2(L^{C2})_3]$-stained vesicles are localized within the endoplasmic reticulum and not in the Golgi apparatus. Estimation of the intracellular concentration by the DELFIA luminescence technique gave about 5×10^8 helicates per cell, or between 0.18 and 0.30 mM, corresponding to a remarkable concentration effect, because cells for this experiment were incubated in the presence of 25 μM of helicate only.

Leakage of the helicates out of the cells was determined with time-lapse experiments and found to be slow as indicated by an approximately 30% loss of luminescence intensity after 24 h. Furthermore, helicates with Sm^{III}, Tb^{III} and Yb^{III} behave in the same way as $[Eu_2(L^{C2})_3]$. Because the luminescence lifetimes are different, some time-based discrimination is therefore feasible, in addition to wavelength discrimination.

The excitation maximum of $[Eu_2(L^{C2})_3]$ at 330 nm is however not optimum, because this wavelength can be potentially phototoxic for some cells. Attempts have therefore been made to shift the excitation wavelength more into the visible. A first solution was to modify the ligand by fusing pyridine rings on the benzimidazole moieties, resulting in H_2L^5 (scheme 1). The resulting self-assembled helicates retain high thermodynamic stability, non-cytotoxicity, and they also localize in the endoplasmic reticulum. Interestingly, their absorption spectra display a low-energy intense band with maxima at 350 and 365 nm ($\log \varepsilon = 4.90$ and 4.82, respectively; figure 10*a*), so that cell experiments can be conveniently performed with excitation at 365 nm, despite a lower quantum yield of 9%. Moreover, confocal microscopy with excitation of $[Eu_2(L^{C5})_3]$ at 405 nm gives brighter images than $[Eu_2(L^{C2})_3]$. The improvement is, however, less than expected: at the latter excitation wavelength, $[Eu_2(L^{C5})_3]$ is much more luminescent than $[Eu_2(L^{C2})_3]$; however, the number of helicates taken up in the cells is 30% lower compared with $[Eu_2(L^{C2})_3]$, which reduces the previous advantage. This demonstrates that all thermodynamic, photophysical and biochemical parameters intervene in defining the efficiency of a given luminescent bioprobe.

Another solution to lengthening the excitation wavelength is to turn to two-photon excitation. The two-photon absorption cross section of $[Eu_2(L^{C5})_3]$ was found to be

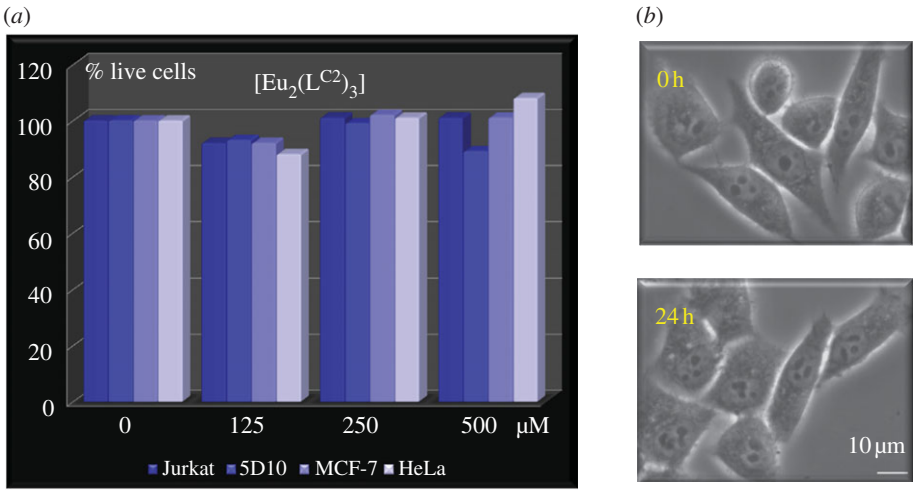

Figure 7. (*a*) Results of WST-1 viability assays for various cell lines incubated for 24 h at 37°C in the presence of various concentrations of $[Eu_2(L^{C2})_3]$. (Reproduced with permission from Chauvin *et al*. [53].) (*b*) Phase contrast images of HeLa cells exposed to 100 μM of $[Eu_2(L^{C2})_3]$. (Adapted from [56].)

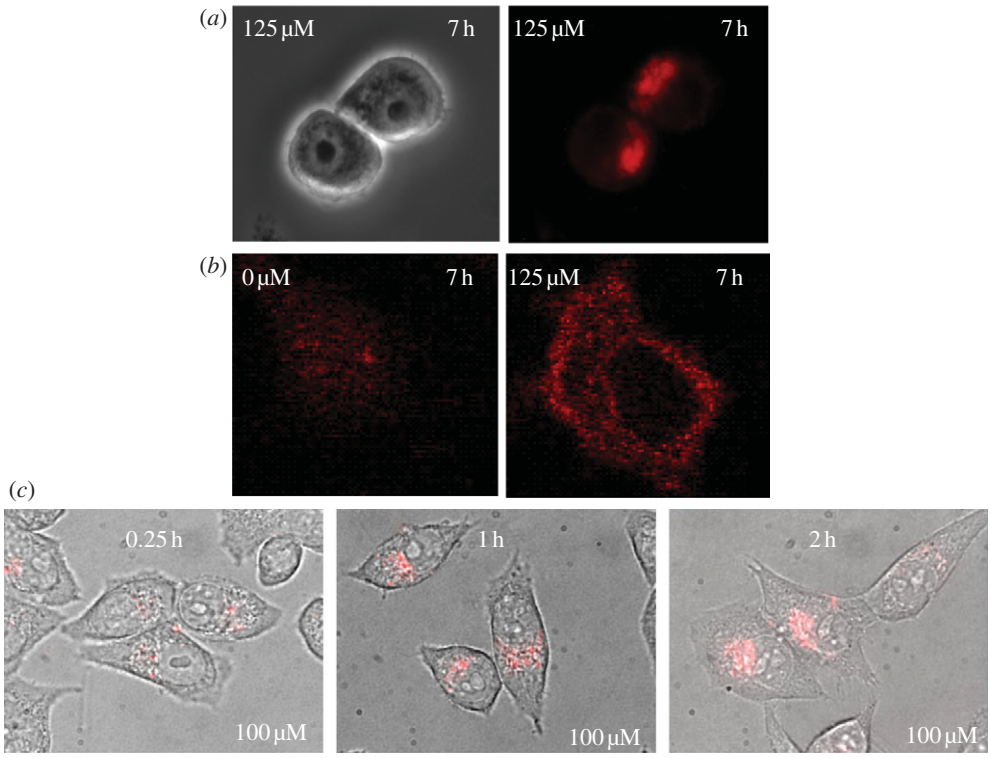

Figure 8. Imaging of HeLa cells incubated at 37°C with $[Eu_2(L^{C2})_3]$. (*a*) Bright-field and luminescence microscopy ($\lambda_{exc} = 330$ nm; exposure time = 60 s). (Unpublished data, 2007.) (*b*) Confocal microscopy ($\lambda_{exc} = 405$ nm). (Adapted from [58].) (*c*) Time-resolved microscopy ($\lambda_{exc} = 330$ nm, time delay = 100 μs; gate time: 600 μs; exposure time: 30 s). (Adapted from [56].)

approximately 9 GM at the maximum of the excitation spectrum (755 nm) and both one-photon and two-photon excitation spectra superimpose perfectly. Despite the small cross section (some Eu^{III} complexes have cross sections up to 775 GM [59]), due to the fact that the ligand is not optimized for multi-photon absorption, well-contrasted images of HeLa cells incubated with 200 μM $[Eu_2(L^{C5})_3]$ could be observed under Ti–sapphire laser excitation at 750 nm [60].

The main drawback of the dinuclear helicates as luminescent bioprobes is their intrinsic lack of selectivity: all tested cell lines are stained in the same way. In principle, one may think that the global charge of a metal complex and/or its lipophilicity can drastically influence its cell cytotoxicity, permeability and localization. We have therefore investigated whether derivatization of the pendant polyoxyethylene moieties and/or modification of the coordination unit would introduce some selectivity or at the least modify the localization of the helicates within the cells. To this end, the ligands shown in scheme 2 have been synthesized. Similar to H_2L^{C2}, they self-assemble with Ln^{III} ions to yield stable dinuclear helicates the photophysical properties of which are modulated by the substituents [61].

These ligands allowed us to test the influence of (i) the coordinating group, phosphonate in $[Eu_2(L^{POEt})_3]$ [62] versus carboxylate in $[Eu_2(L^{C2})_3]$, (ii) the polarity of the pendant arms, OH substituent in $[Eu_2(L^{C_2CH_2OH})_3]$ versus OMe terminal function in $[Eu_2(L^{C2})_3]$) and/or (iii) the overall charge of the probe by using a negatively charged complex

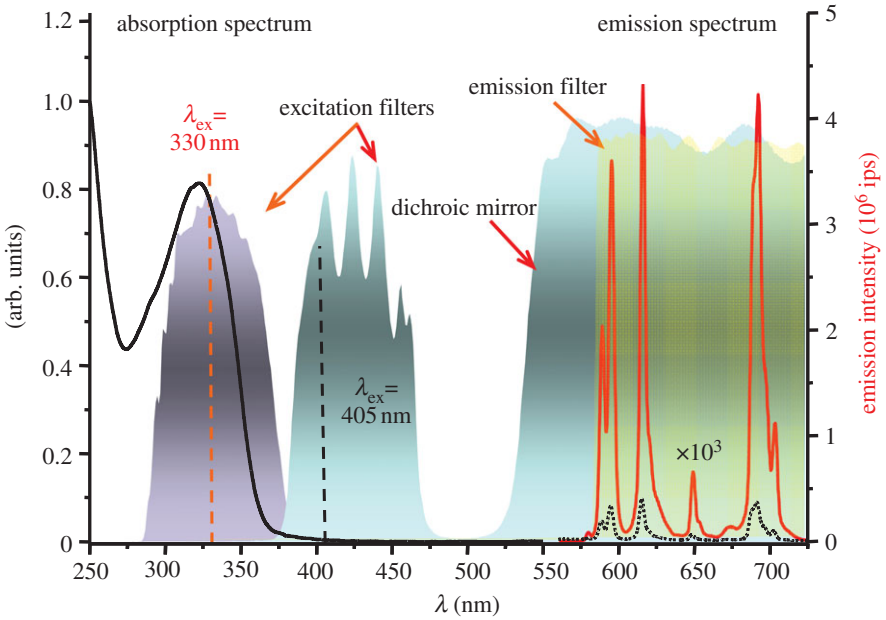

Figure 9. Experimental conditions for luminescence and confocal microscopy. (Reproduced with permission from Chauvin *et al*. [53].)

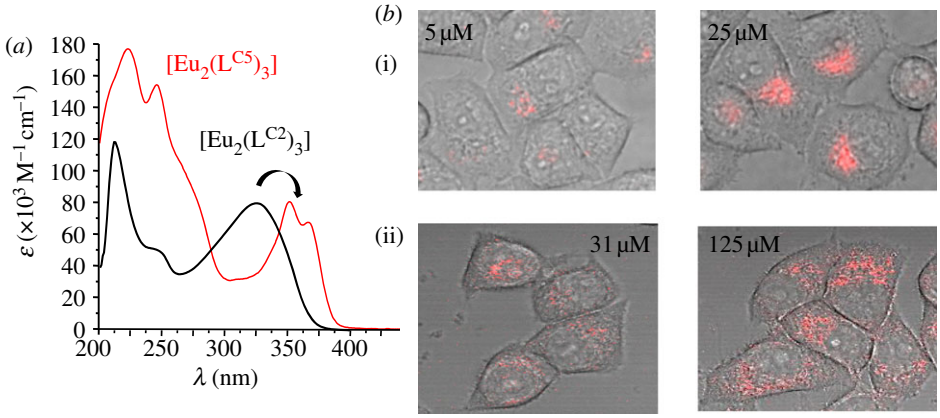

Figure 10. (*a*) Absorption spectra of $[Eu_2(L^{C2})_3]$ and $[Eu_2(L^{C5})_3]$. (Reproduced with permission from [53,57].) (*b*(i)) Time-resolved luminescence images (λ_{exc} 365 nm) of HeLa cells incubated 6 h at 37°C with 5 and 25 μM $[Eu_2(L^{C5})_3]$; (*b*(ii)) confocal microscopy images (λ_{exc} 405 nm) of HeLa cells incubated 18 h at 37°C with 31 and 125 μM $[Eu_2(L^{C5})_3]$. (Adapted from [57].) Copyright ©2009 Wiley-VCH.

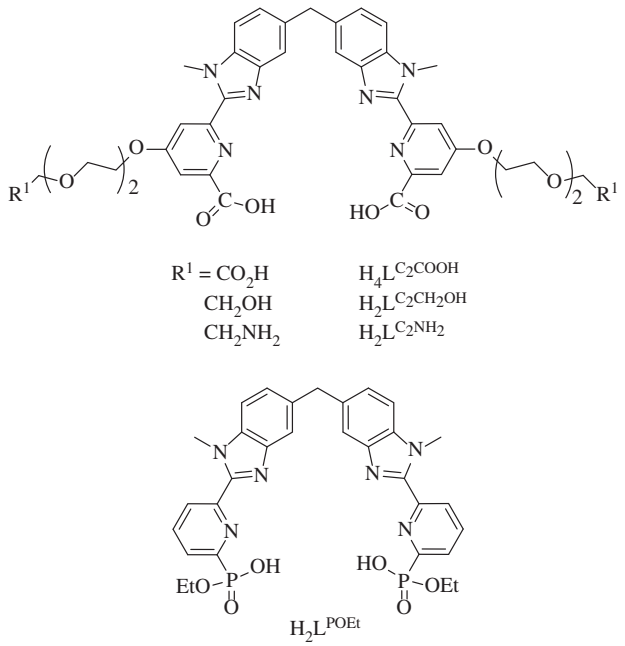

Scheme 2. Derivatized and phosphonate ditopic ligands.

$[Eu_2(L^{C_2COOH}\text{-}2H)_3]^{6-}$ or a potentially positively charged one $[Eu(L^{C_2NH_2}+2H)_3]^{6+}$: indeed, the pH of some endosomal compartments can reach values as low as 2 and, because the pK_b of the terminal amine is around 7.0, it is expected that it will be protonated at such a low pH value. The phosphonate helicate $[Eu_2(L^{POEt})_3]$ was chosen in place of the polyoxyethylene-fitted one because its quantum yield is much larger (25% versus only 2.5%) [62]. All the helicates bearing different coordinating and terminal groups permeate into HeLa cells and stain the cytoplasm. Co-staining experiments with LysoTracker blue show that most helicates are present in secondary endosomes and lysosomes, irrespective of their polarity or overall charge. A similar conclusion has been reached from an extensive study of more than 60 cyclen-based lanthanide luminescent bioprobes; however, for these stains, modification of the nature of the polyaromatic substituent on the cyclen framework led to widely different cell-penetrating properties, localization and cytotoxicity because these substituents are recognized by protein association [14,30,63–65]. As a conclusion, specificity for the dinuclear luminescent probes has to be built via immunochemical reactions.

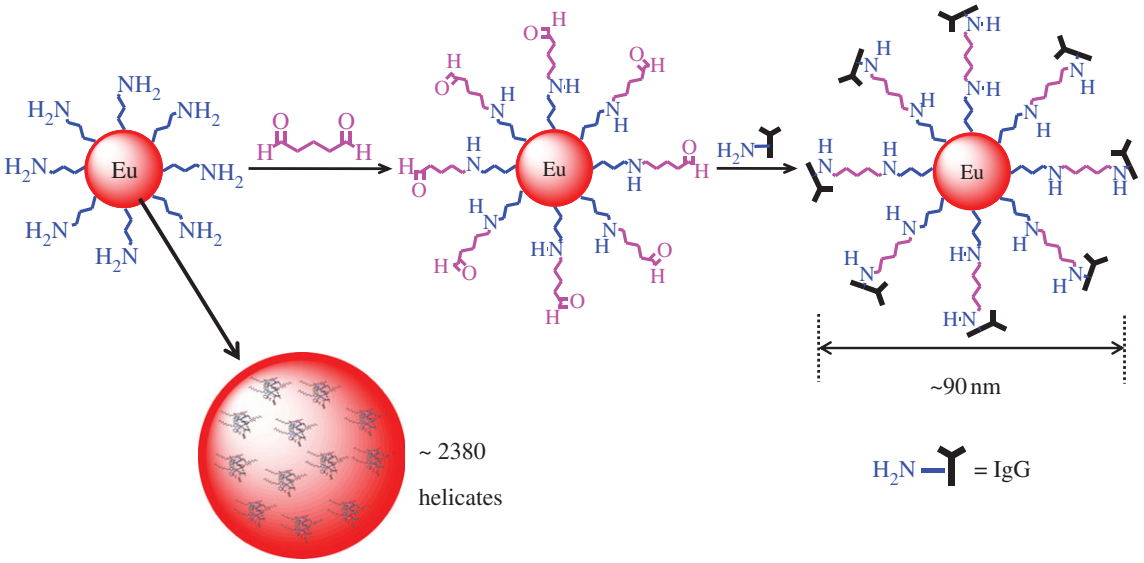

Figure 11. Formation of a bioconjugate between $[Eu_2(L^{C2})_3]@SiO_2/NH_2$ and IgG. (Reproduced with permission from Eliseeva *et al.* [66].)

5. Specific detection of biomarkers

5.1. Bioconjugated nanoparticles

As a first attempt to gain selectivity, $[Eu_2(L^{C2})_3]$ helicates have been imbedded into $-NH_2$ derivatized silica nanoparticles. The resulting nanoparticles, $[Eu_2(L^{C2})_3]@SiO_2/NH_2$, display a larger quantum yield (28%) than the parent helicate and can be conjugated with streptavidin or with monoclonal antibodies (mAbs) [66]. Immunoassays with the nanoparticles derivatized with the goat anti-mouse immunoglobulin G (IgG) mAb (figure 11) were able to detect 15 ng ml^{-1} of the biotinylated 5D10 antibody on a streptavidin-coated plate with a SNR of 100. However, non-specific binding of the derivatized nanoparticles limits the sensitivity of the analysis. Immunocytochemical assays involving recognition of mucin-like proteins expressed on breast cancer MCF-7 cells by the 5D10 mAb led to specific luminescence signals with a SNR approximately 20% larger than the one obtained with the bioconjugate of $[Eu_2(L^{C_2COOH})_3]$ with IgG. In parallel to these assays, we have expanded our quest for biospecificity allied with high detection sensitivity by moving to laboratory-on-a-chip experiments which are described in §5.2.

5.2. Construction and test of a laboratory-on-a-chip device for detecting cancerous cells

Breast cancer accounts for almost one-quarter of cancers affecting women, hence the importance of developing sensitive detection methods. The long-living Michigan Cancer Foundation 7 (MCF-7) cell line, discovered in 1970, is a major cell line used in many studies of this carcinoma. MCF-7 cells can be targeted with use of the 5D10 mAb which reacts with most invasive ductal adenocarcinomas. The diagnostic value of this mAb was established in studies showing that its response to human breast carcinomas correlates with the DNA ploidy status (=the number of sets of chromosomes in the nucleus) of tumour cells [67]. We have therefore developed an indirect immunocytoluminescent assay in which the biotinylated 5D10 mAb is bound to its antigen expressed on the cell membrane and subsequently linked to the avidin-conjugated lanthanide luminescent label. Alternatively, a direct assay can also be conducted in which the detection (primary) mAb is bioconjugated to the luminescent lanthanide helicate. For speeding up the experiment and also, and most importantly, in an effort to reduce cost by reducing the volume of required (expensive) bioconjugates, a simple microfluidics device has been designed which features a 200 µm wide zigzag channel generated by a replica-moulding technique into a block of biocompatible polydimethylsiloxane (PDMS). The device is connected to high precision peristaltic pumps (figure 12).

To test the device, two types of experiments have been implemented (figure 13). In the first one, MCF-7 cells were grown in the fibronectin-coated microchannel and detected in time-resolved mode via the 5D10 mAb test using a commercial lanthanide luminescent probe, Eu-W8044 (scheme 3), with a quantum yield of 23.6(5)% and $Eu(^5D_0)$ lifetime equal to 1.42(2) ms. The attained limit of detection with this bioconjugate (EuB1) was 0.6 µg ml^{-1}, that is 2.3-fold smaller compared with the assay performed with the conjugate of fluorescein isothiocyanate (FiB_3), a common reactant for this type of experiments.

MCF-7 cells express several characteristic receptors among which the oestrogen receptor (ER) expressed by the nucleus membrane and the human epidermal growth factor Her2/*neu* expressed by the cell membrane are particularly important. These two receptors are routinely used in clinical practice, having an established role in predicting tumour response to hormone therapy and to immunotherapy with the mAb trastuzumab used in cancer treatment. The second experiment therefore consisted of detecting these two receptors in three breast cancer tissues (figure 13*b*) which were incubated with anti-Her2/*neu* IgG followed by biotinylated anti-IgG and Eu-W8044-labelled avidin (indirect assay) or with anti-ER IgG followed by Eu-W8044-labelled anti-IgG (direct assay). The cell nuclei were subsequently stained by 4′,6-diamidino-2-phenylindole. The results shown in figure 14 correlate very well with the clinical analyses [68].

The positive outcome of these experiments encouraged us to bioconjugate the $[Ln_2(\mathbf{L}^{C_2COOH})_3]^{6-}$ (Ln = Eu, Tb) helicates and to use the resulting conjugates as luminescent bioprobes for detecting the ER and Her2/*neu* receptors, as described in §5.3.

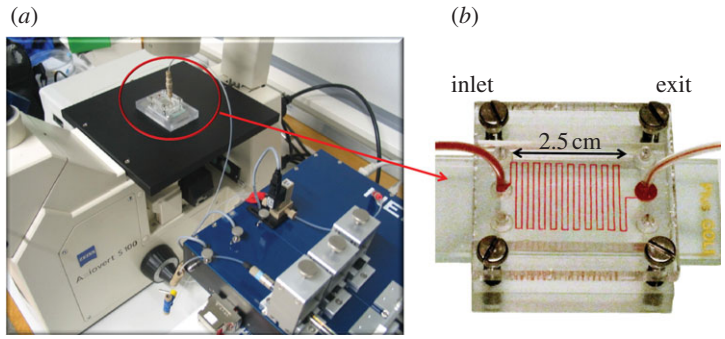

Figure 12. (*a*) Microfluidic device installed on the luminescence microscope with the pumping system on the right-hand side. (*b*) Detail of the zigzag channel. Photographs taken in the author's laboratory.

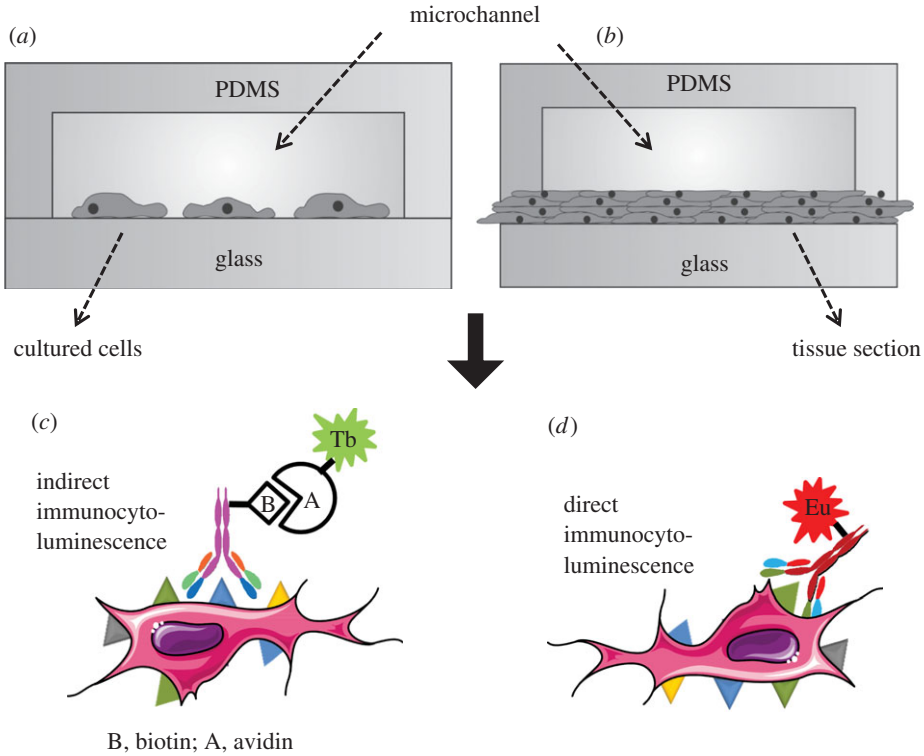

Figure 13. Cross sections of the microfluidic chip used for the study of (*a*) cancer cells seeded in the microchannel and (*b*) a section of human breast cancer tissue. Principles of (*c*) indirect and (*d*) direct immunocytoluminescent assays. (Adapted from [68].) Copyright ©2009 The Royal Society of Chemistry.

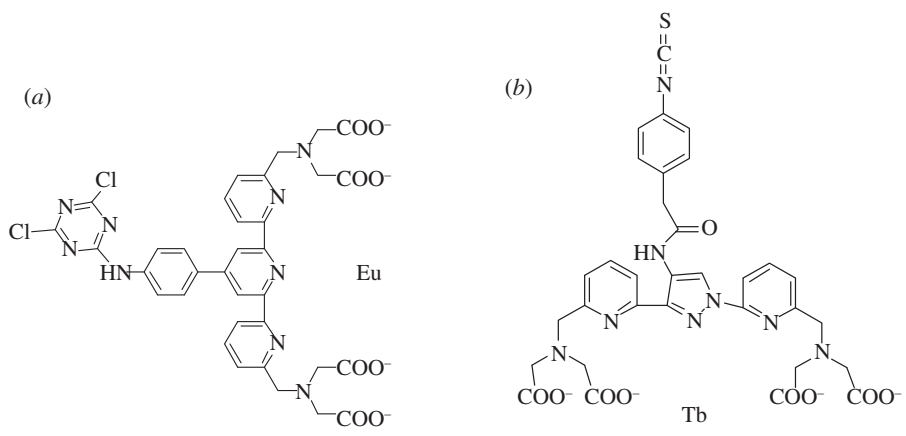

Scheme 3. Formulae of the commercially available (*a*) Eu-W8044 and (*b*) Tb-14016 luminescent chelates.

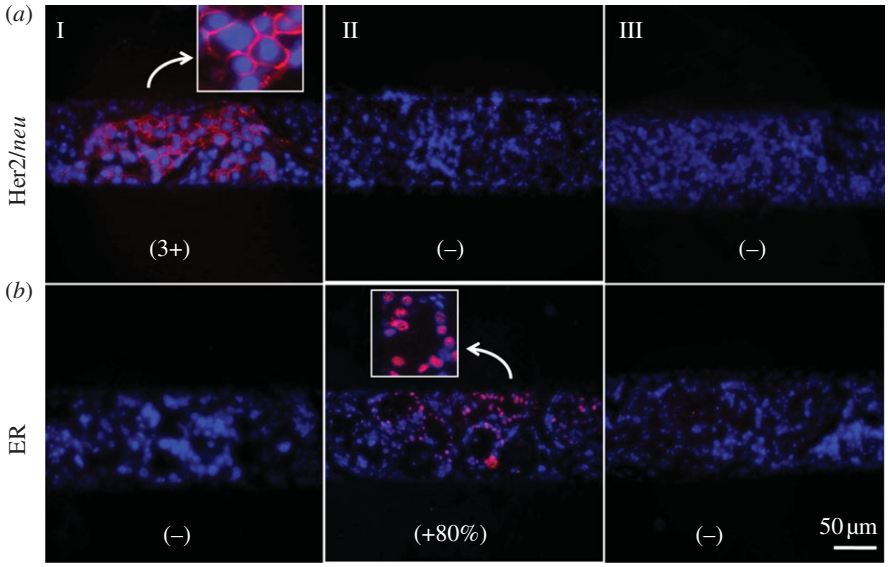

Figure 14. On-chip immunohistochemical detection of Her2/*neu* (*a*) and ER (*b*) in three human breast cancer tissue samples (see text for details). The results of the clinical analyses are given at the bottom: −, negative; 3+, strongly positive; +80%, positive. (Adapted from Song *et al*. [68].) Copyright ©2009 The Royal Society of Chemistry.

5.3. Dinuclear helicates as bioprobes for detecting biomarkers expressed by cancerous cells

The dinuclear $[Eu_2(L^{C_2COOH}\text{-}2H)_3]^{6-}$ helicate was conjugated to avidin in a two-step reaction. First, the carboxylic acid functions of the pendant arms were activated with a mixture of 1-ethyl-3-(3-dimethylaminopropyl)carbodiimide/1-hydroxy-2-nitrobenzene-4-sulfonic acid in dry dimethylsulfoxide. The protein dissolved in phosphate-buffered solution (pH 8.2) was then added, and quenching of the reaction by ethylamine hydrochloride yielded the desired luminescent conjugate EuB2 presenting a statistical repartition of its six arms fitted either with a carboxylate or with carboxamides (CONEt or CON-avidin moieties). On average, 3.2 helicates were found to be bound to avidin, and the covalent nature of this interaction is ascertained by matrix-assisted laser desorption/ionization time of flight (MALDI-TOF) mass spectral data which clearly show a shift of about 3 and 5.9 kDa for two avidin fragments (the helicate has a molar mass of about 3 kDa; figure 15*a*). The photophysical properties of EuB2 are very similar to those of the parent $[Eu_2(L^{C2})_3]$ helicate (table 2), except for the quantum yield which decreases to 9.3%. Owing to the large molar absorption coefficient of the ligands though, the luminosity of this probe remains quite good with $\varepsilon Q = 7560\ M^{-1}\ cm^{-1}$. Bioaffinity assays were performed with EuB1, EuB2, and, for comparison purposes, FiB_3 in the detection of biotinylated rabbit anti-streptavidin (α-SA-B). The results reported in figure 15*b* show the superiority of the Eu-labelled bioconjugates over the fluorescein isothiocyanate one, the detection limits of α-SA-B being 1–2.5 ng μl^{-1} for the Eu^{III} conjugates versus 34 ng μl^{-1} for the all-organic stain.

Similarly, indirect immunocytochemical assays performed on MCF-7 cells revealed that the detection of the mucin-like protein expressed by these cells and evidenced via the biotinylated 5D10 mAb itself recognized by the bioconjugates EuB1, EuB2 and FiB_3 is achieved with better selectivity by the lanthanide bioprobes (SNR = 6–7) compared with the organic one (SNR = 2). The better selectivity of the Eu^{III} bioconjugates is confirmed by statistical analysis of luminescence microscopy images [69]. When MCF-7 cells were grown in the microchannel, the detection limit (DL) is larger, but the lanthanide probes remain more sensitive with DL = 0.6–0.7 versus 1.4 µg ml^{-1}. Finally, the specificity of the 5D10 assay for MCF-7 cells grown in the microchannel is illustrated in figure 16 by TRL microscopy: no Eu^{III} emission is detected when no or the wrong mAb is used or when HeLa cells are reacted with the 5D10 antibody.

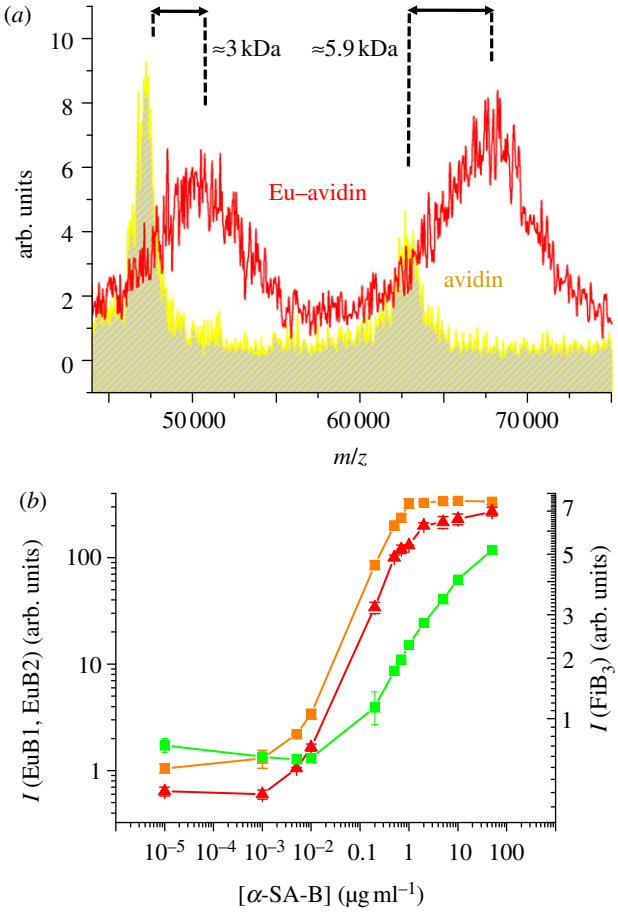

Figure 15. (*a*) Superposition of the MALDI-TOF mass spectra between 45 and 75 kDa of avidin (patterned spectrum) and EuB2 (red line). (*b*) Absolute emission intensity of EuB1 (orange squares), EuB2 (red triangles) and FiB_3 (green squares) as a function of the biotinylated rabbit anti-streptavidin (α-SA-B) antibody concentration. (Reproduced with permission from Fernandez-Moreira *et al*. [69].)

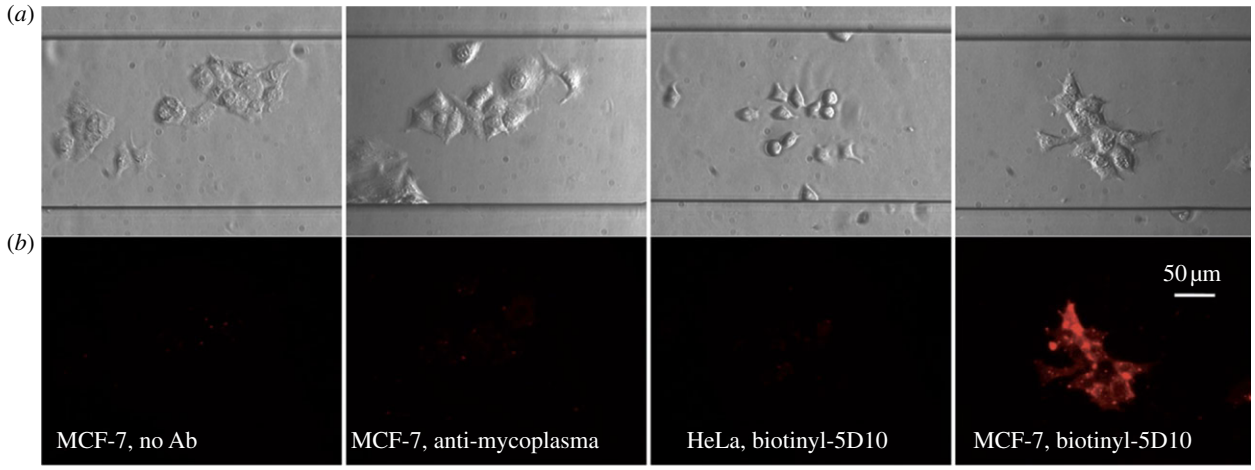

Figure 16. On-chip immunocytochemical detection of the mucin-like protein expressed on MCF-7 cells grown in the 200 µm microchannel by biotinylated 5D10 monoclonal antibody and the EuB2 bioconjugate. (*a*) Bright-field images. (*b*) Time-resolved luminescence images. Columns: negative controls (no mAb, column 1; α-myco-B antibody, column 2; and HeLa cells with 5D10-B, column 3) and positive test with MCF-7 cells and biotinylated 5D10, column 4. (Adapted from Fernendez-Moreira [69].) Copyright ©2010 The Royal Society of Chemistry. (Online version in colour.)

Finally, analysis of the ER and Her2/*neu* receptors expressed in the sections of human breast cancerous tissues has been performed in the microfluidic system similar to what is shown in figure 14, except that both receptors were detected simultaneously by taking advantage of the spectral versatility brought by red-emitting Eu^{III} and green-emitting Tb^{III} bioconjugates. However, when performing the indirect immunohistochemical assays on breast cancer tissues, using the biotin–avidin system, we were confronted with a high intracellular background signal, which can likely be attributed to the intracellular expression of biotin, often observed in cancer tissues. Therefore, two new bioconjugates have been developed: EuB4, a Eu^{III}-labelled goat anti-mouse IgG Ab, and TbB5, a Tb^{III}-labelled goat anti-rabbit IgG Ab. The principle of the indirect immunohistochemical assays is described in figure 17*a* and is alike for both receptors: a primary antibody selective for the targeted receptor is recognized by a secondary antibody conjugated to the chosen lanthanide helicate $[Ln_2(L^{C_2CO_2H})_3]$.

Again, TRD eliminates background noise, yielding highly contrasted images (figure 17*b*). The Her2/*neu* biomarkers expressed on the cancerous cell surface are illuminated by TbB5, whereas the ER biomarkers located within the nuclear membranes of the cancerous cells are evidenced with EuB4. The results are in complete agreement with those obtained in the clinical laboratory using classical immunohistochemistry settings, but were achieved in only 20 min versus the 2 h required for the classical protocol and with five times less reactants. Further analyses of about 50 samples confirmed the match between clinical and TRL analyses. Therefore, this might be good news for health insurances if this new protocol can be effectively implemented, i.e. officially validated.

5.4. Further developments

In order to speed up the previous immunohistochemical detection, another microfluidic device has been designed featuring arrays of microchannels and a 2.5-fold larger detection area. The flush time of the device is considerably shortened, as shown in figure 18*a*: the reactant filling the cell can be flushed (e.g. by a buffer solution) in 2.5 s, its concentration dropping from 1 to 10^{-12} M. With the new analysis chamber which is also easier to assemble and disassemble, the total time of analysis of the Her2/*neu* and ER biomarkers can be completed for each biomarker in less than 5 min, with only 60 µl of reagents and 120 µl of buffer [70].

A common and time-consuming task in biology laboratories is the separation of targeted cells from heterogeneous cell mixtures. Frequently used methods are fluorescence-activated and magnetically activated cell sorting, and these techniques have been adapted to microfluidic environments. However, the continuous flow operation of fluorescence-activated cells bearing an adequate fluorescent tag is not easily compatible with the retention of the targeted cells inside the microfluidic device. On the other hand, in immunomagnetic cell separation, the cells of interest, adequately marked with a magnetic tag, can be retained by activating an external magnetic field. After separation, the cells may be transported to other sites of the microfluidic device for further analysis and/or treatment. The magnetic tag can, however, interfere during these subsequent assay steps and a label-free separation is more desirable. In particular, immunoaffinity-based cell separation represents an interesting method applicable to microfluidic devices.

The tools developed in our laboratories and described above have been combined to produce a protocol in which cell separation, amplification (cell culture) and specific detection are merged in a single set-up. The principle is illustrated in figure 19 and in the following description. First, streptavidin-coated magnetic beads were directly patterned inside a sealed microfluidic channel (width 200 µm, height 100 µm, length 25 mm) by rapid magnetic-field-assisted electrostatic self-assembly (figure 19*a*). The beads, which formed 50 µm wide stripes with a pitch of 40 µm, were then coated with biotinylated 5D10 mAb and biotinylated fibronectin (figure 19*b*) resulting in two-thirds of the bead surface being covered with 5D10 and the remaining surface with fibronectin. The separation concept has been tested with a mixture of MCF-7 and Jurkat cells (figure 19*c*): a single filling step of the microchannel is sufficient to capture all MCF-7 cells, whereas

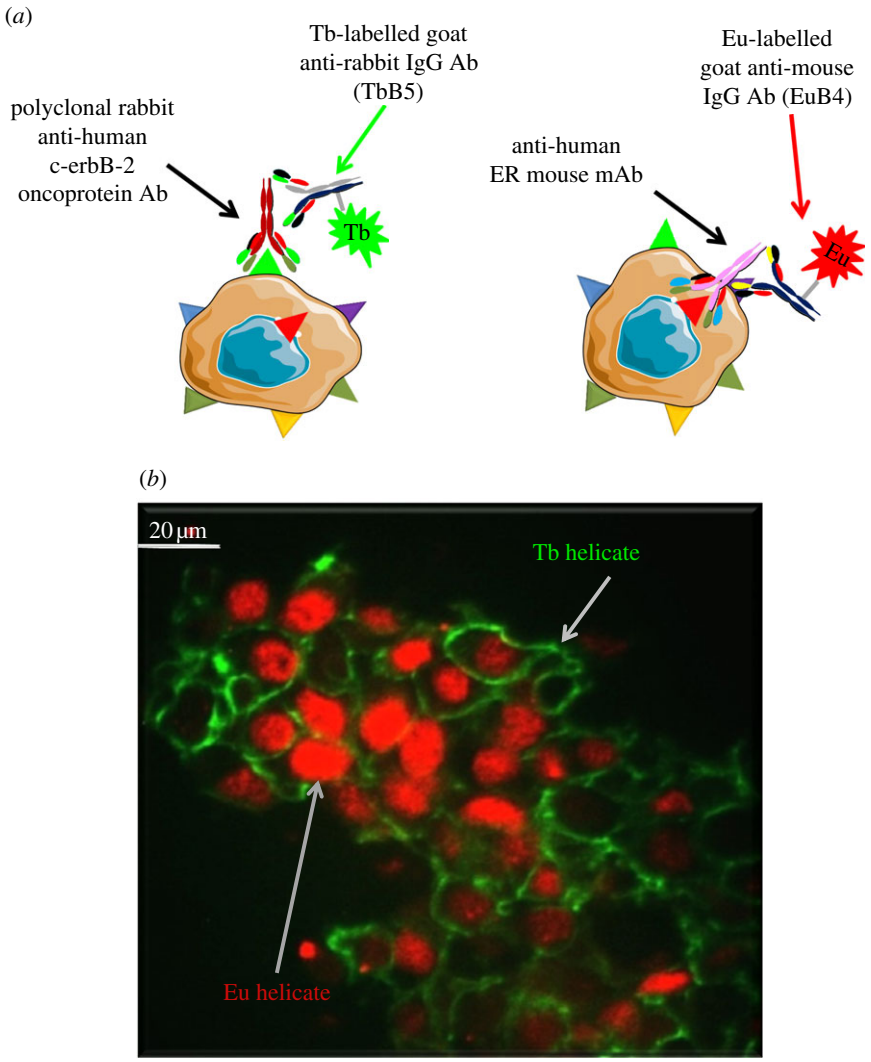

Figure 17. (*a*) Principle of the two indirect assays for the detection of the Her2/*neu* (left) and ER (right) receptors expressed by human breast cancer cells. (*b*) On-chip immunohistochemical detection of Her2/*neu* and ER in a breast cancer tissue sample. (Adapted from Fernandez-Moreira [69].)

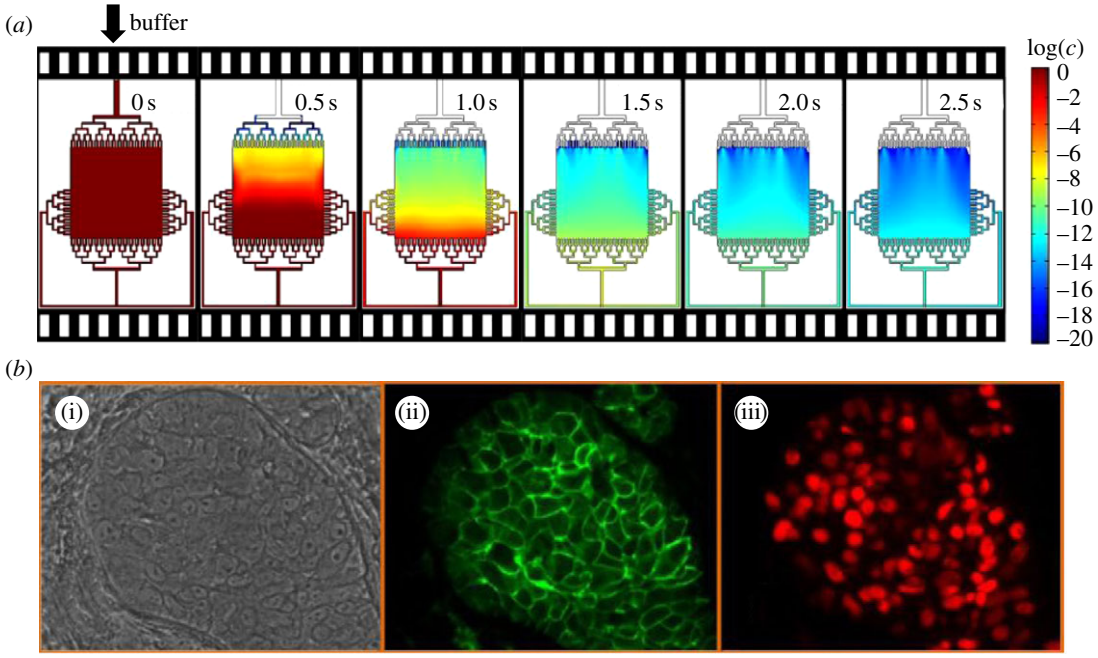

Figure 18. (*a*) Flush time of the second-generation microfluidic chamber. (*b*) Analysis of biomarkers expressed by human breast cancer tissue. (i) Bright-field image; time-resolved luminescence images of the Her2/neu receptors illuminated by the Tb^{III} bioconjugate (ii) and of the ER receptors detected with the Eu^{III} bioconjugate (iii); same experimental conditions as for figure 17. (Adapted from Ciftlik *et al*. [70].)

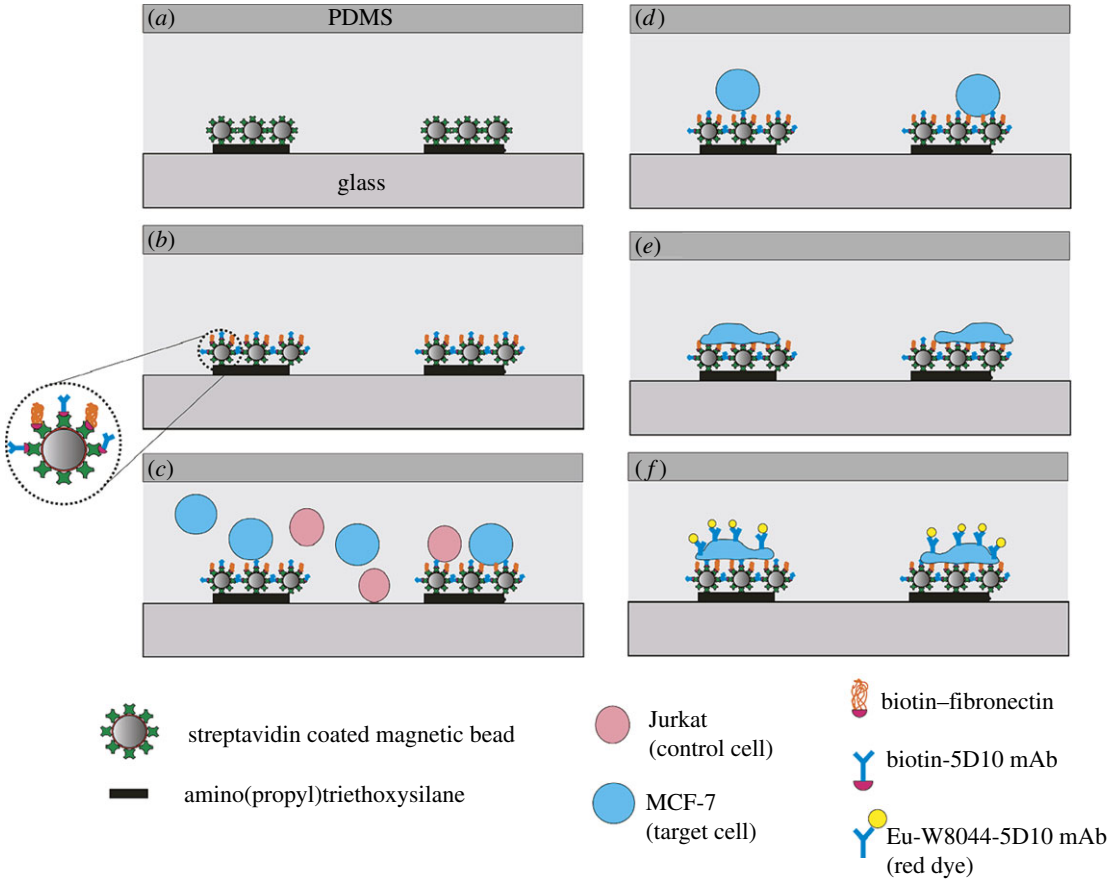

Figure 19. Schematic of the concept of specific capture of MCF-7 cells from a cell mixture on self-assembled beads micropatterned inside a microfluidic channel. See text for explanation. (Adapted from Sivagnanam *et al*. [71].) Copyright ©2010 American Chemical Society.

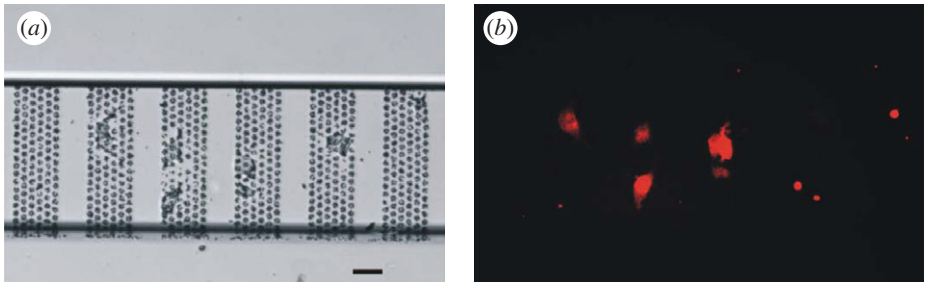

Figure 20. (*a*) Bright-field image showing MCF-7 cells captured and cultured on the patterned beads inside the microchannel device (scale bar, 40 µm). (*b*) Time-resolved luminescent microscopy image showing the presence of the 5D10 biomarkers on the surface of the MCF-7 cells, thanks to the Eu-8044-mAb conjugate. (Adapted from Sivagnanam *et al*. [71].) Copyright ©2010 American Chemical Society.

Jurkat cells are washed out (figure 19*d*). The captured cells were subsequently incubated during 4 h (figure 19*e*) before being detected in time-resolved mode with the commercial Eu^{III}-containing bioconjugate featured in scheme 3 (figure 19*f*). The resulting image is shown in figure 20.

6. Conclusion

The work described in the preceding sections represents only a tiny part of the present efforts devoted to the development of luminescent lanthanide bioprobes displaying high specificity. These efforts are relying on all aspects of lanthanide photophysics, and both coordination compounds and inorganic materials are being investigated, as outlined in §1. The availability of sensitive spectroscopic instrumentation working in the visible and NIR spectral ranges, as well as remarkable improvements in synthetic and surface chemistry allow chemists and biochemists to concentrate on solving specific problems without too many technical restrictions, except for intrinsic physical limits. One of these limits in optical imaging is the penetration depth of light in the tissues. In principle, this may be overcome using NIR light, for example, UCNPs; however, loss of lateral resolution has been observed beyond 600 µm [72], so that improvements are still required. On the other hand, the diversity of luminescent lanthanide ions and compounds thereof is a major asset for tailoring specific analyses using lanthanide bioprobes. There is no doubt that lanthanide bioprobes will remain strong competitors in luminescent immunoassays and that they will add valuable tools to the panoply of techniques available to biochemists and medical doctors for both *in vitro* and *in vivo* bioimaging. Their assets, multiplexing possibility, small photobleaching, non-overlapping excitation and emission spectra, long excited state lifetimes, and easy amenability to

bioconjugation form a unique and highly useful set of properties which cannot be claimed by other bioprobes. In particular, developers in the field are using lanthanide probes in combination with other techniques to produce multi-modal labels each property of which fulfils a specific task. What is also clear is that the full array of diagnostic tools, organic markers, QDs, transition metal and lanthanide bioprobes, as well as biochemical markers, will be necessary to cope with the ever increasing demand for high-quality analyses and images in the biosciences.

Acknowledgements. The author is indebted to all his collaborators for the remarkable work they came up with to develop the dinuclear helical lanthanide bioprobes. Many thanks are extended to Dr I. Hemmilä (Perkin Elmer) and Profs M. Gijs (EPFL), M. Chergui (EPFL) and H.-A. Lehr (CHUV-UNIL) for their efficient input into this work.

Funding statement. Support from the Swiss National Science Foundation (grant no. 20020-119866) and from the Swiss Office for Science and Education (grant no. C07.0116) within the frame of the COST Action D38 from the European Science Foundation is gratefully acknowledged.

References

1. Kelkar SS, Reineke TM. 2011 Theranostics: combining imaging and therapy. *Bioconjugate Chem.* **22**, 1879–1903. (doi:10.1021/bc200151q)
2. Kobayashi H, Longmire MR, Ogawa M, Choyke PL. 2011 Rational chemical design of the next generation of molecular imaging probes based on physics and biology: mixing modalities, colors and signals. *Chem. Soc. Rev.* **40**, 4626–4648. (doi:10.1039/C1CS15077D)
3. Kobayashi H, Choyke PL. 2011 Target-cancer-cell-specific activatable fluorescence imaging probes: rational design and *in vivo* applications. *Acc. Chem. Res.* **44**, 83–90. (doi:10.1021/ar1000633)
4. Ozawa T, Yoshimura H, Kim SB. 2013 Advances in fluorescence and bioluminescence imaging. *Anal. Chem.* **85**, 590–609. (doi:10.1021/ac3031724)
5. Rocha U *et al*. 2013 Subtissue thermal sensing based on neodymium-doped LaF_3 nanoparticles. *ACS Nano* **7**, 1188–1199. (doi:10.1021/nn304373q)
6. Kobayashi H, Ogawa M, Alford R, Choyke PL, Urano Y. 2010 New strategies for fluorescent probe design in medical diagnostic imaging. *Chem. Rev.* **110**, 2620–2640. (doi:10.1021/cr900263j)
7. Drummen GPC. 2012 Fluorescent probes and fluorescence (microscopy) techniques—illuminating biological and biomedical research. *Molecules* **17**, 14 067–14 090. (doi:10.3390/molecules171214067)
8. Meyer T, Begitt A, Vinkemeier U. 2007 Green fluorescent protein-tagging reduces the nucleocytoplasmic shuttling specifically of unphosphorylated STAT1. *FEBS J.* **274**, 815–826. (doi:10.1111/j.1742-4658.2006.05626.x)
9. Zrazhevskiy P, Sena M, Gao X. 2010 Designing multifunctional quantum dots for bioimaging, detection, and drug delivery. *Chem. Soc. Rev.* **39**, 4326–4354. (doi:10.1039/B915139G)
10. Barroso MM. 2011 Quantum dots in cell biology. *J. Histochem. Cytochem.* **59**, 237–251. (doi:10.1369/0022155411398487)
11. Wang Y, Hu R, Lin G, Roy I, Yong KT. 2013 functionalized quantum dots for biosensing and bioimaging and concerns on toxicity. *ACS Appl. Mater. Interface* **5**, 2786–2799. (doi:10.1021/am302030a)
12. Lo KK-W, Choi AW-T, Law WH-T. 2012 Applications of luminescent inorganic and organometallic transition metal complexes as biomolecular and cellular probes. *Dalton Trans.* **41**, 6021–6047. (doi:10.1039/C2DT11892K)
13. Fernandez-Moreira V, Thorp-Greenwood FL, Coogan MP. 2010 Application of d^6 transition metal complexes in fluorescence cell imaging. *Chem. Commun.* **46**, 186–202. (doi:10.1039/b917757d)
14. New EJ, Parker D, Smith DG, Walton JW. 2010 Development of responsive lanthanide probes for cellular applications. *Curr. Opin. Chem. Biol.* **14**, 238–246. (doi:10.1016/j.cbpa.2009.10.003)
15. Bünzli J-CG. 2010 Lanthanide luminescence for biomedical analyses and imaging. *Chem. Rev.* **110**, 2729–2755. (doi:10.1021/cr900362e)
16. Bünzli J-CG, Eliseeva SV. 2013 Intriguing aspects of lanthanide luminescence. *Chem. Sci.* **4**, 1939–1949. (doi:10.1039/C3SC22126A)
17. Bünzli J-CG, Eliseeva SV. 2013 Photophysics of lanthanoid coordination compounds. In *Comprehensive inorganic chemistry II* (ed. VW-W Yam), ch. 8.03. Amsterdam, The Netherlands: Elsevier BV.
18. Demchenko AP. 2013 Nanoparticles and nanocomposites for fluorescence sensing and imaging. *Methods Appl. Fluoresc.* **1**, 022001. (doi:10.1088/2050-6120/1/2/022001)
19. Hemmilä I. 1991 *Applications of fluorescence in immunoassays*, 1st edn. New York, NY: Wiley Interscience.
20. Hemmilä IA. 2008 Time-resolved fluorimetric immunoassays; instrumentation, application, unresolved issues, future trends. In *Springer series on fluorescence. standardization and quality assurance in fluorescence measurements II* (ed. U Resch-Genger), pp. 429–447. Berlin, Germany: Springer.
21. Hagan AK, Zuchner T. 2011 Lanthanide-based time-resolved luminescence immunoassays. *Anal. Bioanal. Chem.* **400**, 2847–2864. (doi:10.1007/s00216-011-5047-7)
22. Bouzigues C, Gacoin T, Alexandrou A. 2011 Biological applications of rare-earth based nanoparticles. *ACS Nano* **5**, 8488–8505. (doi:10.1021/nn202378b)
23. Bae SW, Tan W, Hong JI. 2012 Fluorescent dye-doped silica nanoparticles: new tools for bioapplications. *Chem. Commun.* **48**, 2270–2282. (doi:10.1039/C2CC16306C)
24. Cooper DE, D'Andrea A, Faris GW, MacQueen B, Wright WH. 2007 Up-converting phosphors for detection and identification using antibodies. In *Immunoassay and other bioanalytical techniques* (ed. JM Van Emon), pp. 217–247. Boca Raton, FL: CRC Press, Taylor & Francis.
25. Gorris HH, Wolfbeis OS. 2013 Photon-upconverting nanoparticles for optical encoding and multiplexing of cells, biomolecules, and microspheres. *Angew. Chem. Int. Ed.* **52**, 3584–3600. (doi:10.1002/anie.201208196)
26. Yan B, Boyer JC, Branda NR, Zhao Y. 2011 Near-infrared light-triggered dissociation of block copolymer micelles using upconverting nanoparticles. *J. Am. Chem. Soc.* **133**, 19 714–19 717. (doi:10.1021/ja209793b)
27. Maldiney T *et al*. 2012 *In vivo* optical imaging with rare earth doped $Ca_2Si_5N_8$ persistent luminescence nanoparticles. *Opt. Mater. Express* **2**, 261–268. (doi:10.1364/OME.2.000261)
28. Chen GY, Ohulchanskyy TY, Liu S, Law WC, Wu F, Swihart MT, Agren H, Prasad PN. 2012 Core/shell $NaGdF_4$:Nd^{3+}/$NaGdF_4$ nanocrystals with efficient near-infrared to near-infrared downconversion photoluminescence for bioimaging applications. *ACS Nano* **6**, 2969–2977. (doi:10.1021/nn2042362)
29. D'Aleo A *et al*. 2012 Ytterbium-based bioprobes for near-infrared two-photon scanning laser microscopy imaging. *Angew. Chem. Int. Ed.* **51**, 6622–6625. (doi:10.1002/anie.201202212)
30. Montgomery CP, Murray BS, New EJ, Pal R, Parker D. 2009 Cell-penetrating metal complex optical probes: targeted and responsive systems based on lanthanide luminescence. *Acc. Chem. Res.* **42**, 925–937. (doi:10.1021/ar800174z)
31. Bünzli J-CG. 2013 Luminescence bioimaging with lanthanide complexes. In *Luminescence in lanthanide coordination compounds and nanomaterials* (ed. A de Bettencourt-Dias), ch. 6. Oxford, UK: Wiley-Blackwell.
32. Alcala MA *et al*. 2011 Preferential accumulation within tumors and *in vivo* imaging by functionalized luminescent dendrimer lanthanide complexes. *Biomaterials* **32**, 9343–9352. (doi:10.1016/j.biomaterials.2011.07.076)
33. Jovin TM, Arndt-Jovin DJ. 1989 Luminescence digital imaging microscopy. *Ann. Rev. Biophys. Biophys. Chem.* **18**, 271–308. (doi:10.1146/annurev.biophys.18.1.271)
34. Weissleder R, Ntziachristos V. 2003 Shedding light onto live molecular targets. *Nat. Med.* **9**, 123–128. (doi:10.1038/nm0103-123)
35. Shia V, Watt D, Faris GW. 2011 High-speed camera with real time processing for frequency domain imaging. *Biomed. Opt. Express* **2**, 1931–1945. (doi:10.1364/BOE.2.001931)

36. Jin DY, Piper JA. 2011 Time-gated luminescence microscopy allowing direct visual inspection of lanthanide-stained microorganisms in background-free condition. *Anal. Chem.* **83**, 2294–2300. (doi:10.1021/ac103207r)
37. Connally R, Jin DY, Piper J. 2006 High intensity solid-state UV source for time-gated luminescence microscopy. *Cytometry A* **69**, 1020–1027. (doi:10.1002/cyto.a.20326)
38. Bernardinelli G, Piguet C, Williams AF. 1992 The first self-assembled dinuclear triple-helical lanthanide complex: synthesis and structure. *Angew. Chem. Int. Ed.* **31**, 1622–1624. (doi:10.1002/anie.199216221)
39. André N, Jensen TB, Scopelliti R, Imbert D, Elhabiri M, Hopfgartner G, Piguet C, Bünzli J-CG. 2004 Supramolecular recognition of heteropairs of lanthanide ions: a step toward self-assembled bifunctional probes. *Inorg. Chem.* **43**, 515–529. (doi:10.1021/ic0351996)
40. Jensen TB, Scopelliti R, Bünzli J-CG. 2008 Tuning the self-assembly of lanthanide triple stranded heterobimetallic helicates by ligand design. *Dalton Trans.* 1027–1036. (doi:10.1039/b715672c)
41. Piguet C, Hopfgartner G, Williams AF, Bünzli J-CG. 1995 Self-assembly of the first heterodinuclear d–f triple helix in solution. *J. Chem. Soc. Chem. Commun.* 491–493. (doi:10.1039/c39950000491)
42. Piguet C, Edder C, Rigault S, Bernardinelli G, Bünzli J-CG, Hopfgartner G. 2000 Isolated d–f pairs in supramolecular complexes with tunable structural and electronic properties. *J. Chem. Soc. Dalton Trans.* 3999–4006. (doi:10.1039/b003521l)
43. Piguet C, Bünzli J-CG. 2010 Self-assembled lanthanide helicates: from basic thermodynamics to applications. In *Handbook on the physics and chemistry of rare earths*, vol. 40 (eds KA Gschneidner, J-CG Bünzli, VK Pecharsky), ch. 247, pp. 301–553. Amsterdam, The Netherlands: Elsevier Science BV.
44. Canard G, Piguet C. 2007 The origin of the surprising stabilities of highly charged self-assembled polymetallic complexes in solution. *Inorg. Chem.* **46**, 3511–3522. (doi:10.1021/ic062126o)
45. Elhabiri M, Scopelliti R, Bünzli J-CG, Piguet C. 1998 The first lanthanide-containing helicates self-assembled in water. *Chem. Commun.* 2347–2349. (doi:10.1039/A806730l)
46. Elhabiri M, Scopelliti R, Bünzli J-CG, Piguet C. 1999 Lanthanide helicates self-assembled in water: a new class of highly stable and luminescent dimetallic carboxylates. *J. Am. Chem. Soc.* **121**, 10 747–10 762. (doi:10.1021/ja991854q)
47. Elhabiri M, Hamacek J, Humbert N, Bünzli J-CG, Albrecht-Gary A-M. 2004 Proton-assisted dissociation of a triple-stranded dinuclear europium helicate. *New J. Chem.* **28**, 1096–1099. (doi:10.1039/b405934d)
48. Martin N, Bünzli J-CG, McKee V, Piguet C, Hopfgartner G. 1998 Self-assembled dinuclear lanthanide helicates: substantial luminescence enhancement upon replacing terminal benzimidazole groups by carboxamide binding units. *Inorg. Chem.* **37**, 577–589. (doi:10.1021/ic971401r)
49. Bünzli J-CG, Chauvin A-S, Vandevyver CDB, Song B, Comby S. 2008 Lanthanide bimetallic helicates for *in vitro* imaging and sensing. *Ann. NY Acad. Sci.* **1130**, 97–105. (doi:10.1196/annals.1430.010)
50. Gonçalves e Silva FR, Malta OL, Reinhard C, Güdel HU, Piguet C, Moser JE, Bünzli J-CG. 2002 Visible and near-infrared luminescence of lanthanide-containing dimetallic triple-stranded helicates: energy transfer mechanisms in the Sm(III) and Yb(III) molecular edifices. *J. Phys. Chem. A* **106**, 1670–1677. (doi:10.1021/jp012884u)
51. Cantuel M, Bernardinelli G, Muller G, Riehl JP, Piguet C. 2004 The first enantiomerically pure helical noncovalent tripod for assembling nine-coordinate lanthanide(III) podates. *Inorg. Chem.* **43**, 1840–1849. (doi:10.1021/ic035292u)
52. Chauvin A-S, Comby S, Song B, Vandevyver CDB, Bünzli J-CG. 2007 A polyoxyethylene-substituted bimetallic europium helicate for luminescent staining of living cells. *Chem. Eur. J.* **13**, 9515–9526. (doi:10.1002/chem.200700883)
53. Chauvin A-S, Comby S, Song B, Vandevyver CDB, Bünzli J-CG. 2008 A versatile ditopic ligand system for sensitizing the luminescence of bimetallic lanthanide bio-imaging probes. *Chem. Eur. J.* **14**, 1726–1739. (doi:10.1002/chem.200701357)
54. Deiters E, Song B, Chauvin A-S, Vandevyver CDB, Bünzli J-CG. 2008 Testing the length of the pyridine substituent on cellular uptake in a bimetallic europium luminescent probe. *New J. Chem.* **32**, 1140–1152. (doi:10.1039/b800516h)
55. Song B, Vandevyver CDB, Deiters E, Chauvin A-S, Hemmilä IA, Bünzli J-CG. 2008 A versatile method for quantification of DNA and PCR products based on time-resolved Eu^{III} luminescence. *Analyst* **133**, 1749–1756. (doi:10.1039/b807959e)
56. Song B, Vandevyver CDB, Chauvin A-S, Bünzli J-CG. 2008 Time-resolved luminescence microscopy of bimetallic lanthanide helicates in living cells. *Org. Biomol. Chem.* **6**, 4125–4133. (doi:10.1039/B811427G)
57. Deiters E, Song B, Chauvin A-S, Vandevyver C, Bünzli J-CG. 2009 Luminescent bimetallic lanthanide bioprobes for cellular imaging with excitation into the visible. *Chem. Eur. J.* **15**, 885–900. (doi:10.1002/chem.200801868)
58. Vandevyver CDB, Chauvin A-S, Comby S, Bünzli J-CG. 2007 Luminescent lanthanide bimetallic triple-stranded helicates as potential cellular imaging probes. *Chem. Commun.* 1716–1718.
59. D'Aléo A, Picot A, Baldeck PL, Andraud C, Maury O. 2008 Design of dipicolinic acid ligands for the two-photon sensitized luminescence of europium complexes with optimized cross-sections. *Inorg. Chem.* **47**, 10 269–10 279. (doi:10.1021/ic8012975)
60. Eliseeva SV, Auböck G, van Mourik F, Cannizo A, Song B, Deiters E, Chauvin A-S, Chergui M, Bünzli J-CG. 2010 Multiphoton-excited luminescent lanthanide bioprobes: two- and three-photon cross sections of dipicolinates derivatives and binuclear helicates. *J. Phys. Chem. B* **114**, 2932–2937. (doi:10.1021/jp9090206)
61. Chauvin A-S, Thomas F, Song B, Vandevyver CDB, Bünzli J-CG. 2013 Synthesis and cell localization of self-assembled dinuclear lanthanide bioprobes. *Phil. Trans. R. Soc. A* **371**, 20120295. (doi:10.1098/rsta.2012.0295)
62. Chauvin A-S, Comby S, Baud M, De Piano C, Duhot C, Bünzli J-CG. 2009 Luminescent lanthanide helicates self-assembled from ditopic ligands bearing phosphonic acid or phosphoester units. *Inorg. Chem.* **48**, 10 687–10 696. (doi:10.1021/ic901424w)
63. Murray BS, New EJ, Pal R, Parker D. 2008 Critical evaluation of five emissive europium(III) complexes as optical probes: correlation of cytotoxicity, anion and protein affinity with complex structure, stability and intracellular localisation profile. *Org. Biomol. Chem.* **6**, 2085–2094. (doi:10.1039/b803895c)
64. Poole RA, Montgomery CP, New EJ, Congreve A, Parker D, Botta M. 2007 Identification of emissive lanthanide complexes suitable for cellular imaging that resist quenching by endogenous anti-oxidants. *Org. Biomol. Chem.* **5**, 2055–2062. (doi:10.1039/b705943d)
65. Yu JH, Parker D, Pal R, Poole RA, Cann MJ. 2006 A europium complex that selectively stains nucleoli of cells. *J. Am. Chem. Soc.* **128**, 2294–2299. (doi:10.1021/ja056303g)
66. Eliseeva SV, Song B, Vandevyver CDB, Chauvin A-S, Wacker JB, Bünzli J-CG. 2010 Increasing the efficiency of lanthanide luminescent bioprobes: bioconjugated silica nanoparticles as markers for cancerous cells. *New J. Chem.* **34**, 2915–2921. (doi:10.1039/C0NJ00440E)
67. Chin Y, Plessers L, Vandepitte J, Raus J. 1991 A murine monoclonal antibody to human breast cancer cells associated with DNA ploidy status. *Eur. J. Cancer* **27**, 48–50. (doi:10.1016/0277-5379(91)90059-M)
68. Song B, Sivagnanam V, Vandevyver CDB, Hemmilä IA, Lehr H-A, Gijs MAM, Bünzli J-CG. 2009 Time-resolved lanthanide luminescence for lab-on-a-chip detection of biomarkers on cancerous tissues. *Analyst* **134**, 1991–1993. (doi:10.1039/b911301k)
69. Fernandez-Moreira V, Song B, Sivagnanam V, Chauvin A-S, Vandevyver CDB, Gijs MAM, Hemmilä IA, Lehr H-A, Bünzli J-CG. 2010 Bioconjugated lanthanide luminescent helicates as multilabels for lab-on-a-chip detection of cancer biomarkers. *Analyst* **135**, 42–52. (doi:10.1039/b922124g)
70. Ciftlik AT, Song B, Vandevyver CDB, Bünzli J-CG, Lehr H-A, Gijs MAM. 2010 Fast immunohistochemical biomarker detection device for cancer tissue slices. In *Proc. 14th Int. Conf. Miniaturized Systems for Chemistry and Life Sciences, Groningen, The Netherlands, 3–7 October 2010*, pp. 699–701. Cambridge, UK: Royal Society of Chemistry.
71. Sivagnanam V, Song B, Vandevyver CDB, Bünzli J-CG, Gijs MAM. 2010 Selective breast cancer cell capture, culture, and immunocytochemical analysis using self-assembled magnetic bead patterns in a microfluidic chip. *Langmuir* **26**, 6091–6096. (doi:10.1021/la9045572)
72. Pichaandi J, Boyer JC, Delaney KR, van Veggel FCJM. 2011 Two-photon upconversion laser (scanning and wide-field) microscopy using Ln^{3+}-doped $NaYF_4$ upconverting nanocrystals: a critical evaluation of their performance and potential in bioimaging. *J. Phys. Chem. C* **115**, 19 054–19 064. (doi:10.1021/jp206345j)